The transition from complex craters to multi-ring basins on the Moon: Quantitative geometric properties from Lunar Reconnaissance Orbiter Lunar Orbiter Laser Altimeter (LOLA) data

The transition from complex craters to multi-ring basins on the Moon: Quantitative geometric properties from Lunar Reconnaissance Orbiter Lunar Orbiter Laser Altimeter (LOLA) data

David M. H. Baker,[1] James W. Head,[1] Gregory A. Neumann,[2] David E. Smith,[2,3] and Maria T. Zuber[2,3]

Received 31 October 2011; revised 22 January 2012; accepted 23 January 2012; published 22 March 2012.

[1] The morphologic transition from complex impact craters, to peak-ring basins, and to multi-ring basins has been well-documented for decades. Less clear has been the morphometric characteristics of these landforms due to their large size and the lack of global high-resolution topography data. We use data from the Lunar Orbiter Laser Altimeter (LOLA) instrument onboard the Lunar Reconnaissance Orbiter (LRO) spacecraft to derive the morphometric characteristics of impact basins on the Moon, assess the trends, and interpret the processes involved in the observed morphologic transitions. We first developed a new technique for measuring and calculating the geometric/morphometric properties of impact basins on the Moon. This new method meets a number of criteria that are important for consideration in any topographic analysis of crater landforms (e.g., multiple data points, complete range of azimuths, systematic, reproducible analysis techniques, avoiding effects of post-event processes, robustness with respect to the statistical techniques). The resulting data more completely capture the azimuthal variation in topography that is characteristic of large impact structures. These new calculations extend the well-defined geometric trends for simple and complex craters out to basin-sized structures. Several new geometric trends for peak-ring basins are observed. *Basin depth:* A factor of two reduction in the depth to diameter (d/D_r) ratio in the transition from complex craters to peak-ring basins may be characterized by a steeper trend than known previously. The d/D_r ratio for peak-ring basins decreases with rim-crest diameter, which may be due to a non-proportional change in excavation cavity growth or scaling, as may occur in the simple to complex transition, or increased magnitude of floor uplift associated with peak-ring formation. *Wall height, width, and slope:* Wall height and width increase with increasing rim-crest diameter, while wall slope decreases; decreasing ratios of wall width to radius and wall height to depth may reflect burial of wall slump block toes by impact melt redistribution during transient cavity collapse. Melt expulsion from the central basin may help to explain the observed increase in floor height to depth ratio; such central depressions are seen within the largest peak-ring basins. *Peak-ring height:* Heights of peak rings increase with increasing rim-crest diameter (similar to central peak heights in complex craters); peak-ring height to basin depth ratio also increases, suggesting that floor uplift is even larger in magnitude in the largest peak-ring basins. No correlation is found between peak-ring elevation and distance to the rim wall within a single basin, suggesting that rim-wall slumping does not control the topography of peak rings. *Offset of peak rings*: Peak rings often show minor offset from the basin center. Enhancement in peak-ring elevation in the direction of offset is generally not observed, although this could be a function of magnitude of offset. *Basin volume*: Volumes of peak-ring basins are about 40% smaller than the volumes predicted by geophysical estimates of the dimensions of

[1]Department of Geological Sciences, Brown University, Providence, Rhode Island, USA.
[2]Solar System Exploration Division, NASA Goddard Space Flight Center, Greenbelt, Maryland, USA.
[3]Department of Earth, Atmospheric and Planetary Sciences, MIT, Cambridge, Massachusetts, USA.

0148-0227/12/2011JE004021

corresponding excavation cavities. This difference indicates that collapse of the transient cavity must result in large inward and upward translations of the cavity floor. These new observations of geometric/morphometric properties of protobasins and peak-ring basins place some constraints on the processes controlling the onset and formation of interior landforms in peak-ring basins. Comparisons of the geometric trends of the inner rings of Orientale basin with those of peak-ring basins are generally consistent with a mega-terrace model for the formation of multi-ring basins.

Citation: Baker, D. M. H., J. W. Head, G. A. Neumann, D. E. Smith, and M. T. Zuber (2012), The transition from complex craters to multi-ring basins on the Moon: Quantitative geometric properties from Lunar Reconnaissance Orbiter Lunar Orbiter Laser Altimeter (LOLA) data, *J. Geophys. Res.*, *117*, E00H16, doi:10.1029/2011JE004021.

1. Introduction

[2] Our understanding of the processes controlling the evolution of crater landforms on planetary bodies has relied on detailed morphologic and topographic analyses. It has been well documented on the Moon and the terrestrial planets that there is an evolution of crater morphologies with increasing size of the impact structure [*Baldwin*, 1963; *Hartmann and Wood*, 1971; *Howard*, 1974; *Wood and Head*, 1976]. At the largest crater sizes, complex craters exhibiting prominent wall terracing and central peaks transition to peak-ring basins characterized by a single interior ring of peaks. This transition then ends with the largest impact events, which form multi-ring basins displaying more than two concentric topographic rings. Although less numerous, additional basin morphological types in the transition from complex craters to peak-ring basins have been recognized. These include protobasins, with both a central peak and peak ring and ringed peak-cluster basins, which display ring-like arrangements of central peaks that are much smaller in diameter than those in peak-ring basins of the same rim-crest diameter [*Pike*, 1988; *Schultz*, 1988; *Baker et al.*, 2011a, 2011b]. Morphological measurements of the rim-crest and ring diameters of protobasins, peak-ring basins and multi-ring basins have provided much insight into the basin formation process [*Pike and Spudis*, 1987; *Pike*, 1988; *Alexopoulos and McKinnon*, 1994; *Baker et al.*, 2011a]. Measurements of the topographic properties of basins (e.g., depth, height of central peak and peak ring, wall height and width) have also been important in understanding the processes controlling the excavation and modification of the transient cavity during large impact events [*Pike*, 1977, 1988; *Melosh*, 1989; *Spudis*, 1993]. However, due to the limitations in the available data sets, the topographic characteristics of impact basins have historically been difficult to quantify accurately.

[3] The earliest comprehensive topographic characterizations of craters on the Moon have relied on image photoclinometry and stereo-photogrammetry [e.g., *Baldwin*, 1963; *Pike*, 1976]. More recent digital elevation models (DEMs) of the lunar surface provided by several laser rangers/altimeters have substantially improved our understanding of the topography of lunar craters. The Lunar Orbiter Laser Altimeter (LOLA) instrument onboard the Lunar Reconnaissance Orbiter (LRO) [*Smith et al.*, 2010] is currently providing global gridded topographic models of the lunar surface at a maximum resolution of 1024 ppd (~30 m/pixel), a several orders of magnitude improvement over prior DEMs of the Moon (e.g., Clementine lidar DEMs at 8–30 km/pixel [*Smith et al.*, 1997] and DEMs from the Kaguya Laser Altimeter at ~2 km/pixel [*Araki et al.*, 2009]). The improved resolution of LOLA is due to its relatively higher spatial density of altimetry measurements over the entire lunar globe, which is systematically improving with time in orbit. The availability of this vastly improved data set thus provides the opportunity to quantify more accurately the geometric properties of basins in the transition from complex craters to peak-ring basins and to multi-ring basins on the Moon.

[4] Here, we describe new techniques for calculating various geometric properties of basins from DEMs, such as those from LOLA. These techniques can be applied to any planetary body with high-quality DEMs and can be modified for different crater morphology classes. We concentrate on peak-ring basins and protobasins specifically, as these features have traditionally been poorly characterized due to the difficulties of obtaining accurate shadow measurements of their long-wavelength, subtle topography and because of their complex interior morphologies. Furthermore, recently updated catalogs of lunar and mercurian peak-ring basins and protobasins [*Baker et al.*, 2011a, 2011b] provide improved rim-crest and peak-ring diameter measurements that we can use as a foundation for further quantitative characterization. The goal of these analyses is to ultimately calculate a set of geometric properties for peak-ring basins and protobasins that can be used to test models of the peak-ring and multi-ring basin formation process.

2. Background on Lunar Topography Data

[5] The geometric properties of lunar craters and basins derived from topography of the Moon have been the subject of study for decades. Early comprehensive quantification of lunar crater topography used contour maps derived from photoclinometry of Earth-based telescopic images [*Baldwin*, 1963]. Subsequent orbital image data from the Lunar Orbiter in the late 1960s and images from the Apollo metric camera accompanying the Apollo missions in the 1970s, greatly facilitated new quantitative analyses of the topography of craters through photoclinometry and stereophotogrammetry (e.g., Lunar Topographic Orthomaps (LTOs), [*Schimerman*, 1973]). Measurements of the geometric properties of hundreds of fresh craters on the Moon using these improved data products were pioneered by R. J. Pike [e.g., *Pike*, 1976] and still provide the foundation for many current models of impact crater formation. However, due to the limited spatial coverage of Lunar Topographic Orthomaps and the large-scale, subtle topography of the largest craters, only the smallest craters with the best image coverage and illumination geometries could be analyzed. Thus, the geometric

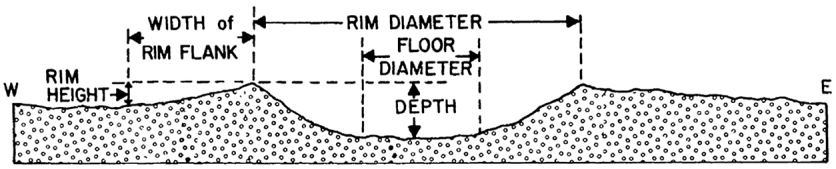

Figure 1. Major geometric properties of craters calculated by *Pike* [1976] for craters on the Moon [from *Pike*, 1976].

properties of complex craters and larger basins with complex interior topography have been the most difficult to quantify.

[6] Global characterization of crater geometries has been facilitated with more recently acquired global laser ranging data and derived gridded DEMs. In 1994, the Clementine lidar instrument provided topographic data along individual tracks separated by ~60 km at the equator and less elsewhere, with a north-south shot spacing along individual tracks of 20 km assuming a 100% pulse detection rate [*Smith et al.*, 1997]. Unfortunately, due to the lack of optimization of the lidar's receiver function during its ranging sequence, the instrument had many missed detections and false returns, detecting only 19% of returned pulses, with about 36% of these attributed to noise [*Zuber et al.*, 1994; *Smith et al.*, 1997; *Williams and Zuber*, 1998]. As a result, along-track shot spacing was more typically of the order of 100 km during a single orbital pass; smaller shot spacings as little as 4 km were achieved as the number of orbital passes increased over the course of the mission. While orbital shots were gridded into a 0.25° by 0.25° (~8 km by 8 km) DEM for latitudes between 79°S to 82°N, much interpolation between the large track spacing was necessary, resulting in high uncertainty in topography within these regions [*Smith et al.*, 1997]. For this reason, more reliable geometric characterization of craters and basins using Clementine lidar has used individual tracks [*Williams and Zuber*, 1998].

[7] With the current high spatial density of laser shots from the LOLA instrument—nearly 4.9 billion as of this writing—derived global DEMs of the lunar surface are substantially improved in resolution and reliability. There are now global LOLA DEMs of the lunar surface at a remarkable 1024 pixels per degree (ppd) (~30 m/pixel) resolution. While gaps in spatial coverage of laser tracks still exist, leading to necessary interpolation steps when producing LOLA DEMs, these gaps are orders of magnitude smaller than the ~60 km gaps of Clementine lidar tracks and are being filled systematically. The accuracy of individual radial measurements from LOLA is 1–2 m with respect to the center of mass of the Moon; however, the lunar potential is uncertain by as much as 20 m on the lunar farside. As a result of these uncertainties, it is customary for DEMs to use a spherical datum (IAU2006), where slopes are measured with respect to a planetocentric radial vector, not the local vertical. Errors in slope introduced by this assumption arise mainly from the equator-to-pole flattening, but may locally be as large as 0.14 degrees at the rims of mare basins.

3. Previous Methods of Topographic Measurements

[8] Manual topographic measurements of hundreds of craters is a tedious process, increasing in time and complexity with increasing crater size. *Pike* [1976] laboriously measured a number of geometric properties for hundreds of fresh craters on the Moon using Lunar Orbiter (LO) images and Lunar Topographic Orthomaps (LTOs). Five main properties were identified that were viewed as accurately characterizing the overall surface geometry of lunar craters (Figure 1): rim-crest diameter, width and height of the exterior rim flank, diameter of the flat inner floor, and depth (Figure 1). From these measured properties, several other geometries were calculated, including slope of the exterior rim flank, width and slope of the interior wall between the rim crest and crater floor, and depth of the crater below the pre-crater datum. For consistency with this widely cited study on crater geometries, we use mostly the same nomenclature and include similar measurements herein (see section 4 and Figure 2). For details on how these early crater measurements were made, the reader is referred to the description by *Pike* [1976].

[9] A major difficulty in calculating geometric properties of large craters has been accounting for their substantial azimuthal variation in topography, which appears to increase in complexity with increasing crater size [*Pike*, 1974, 1976, 1977; *Settle and Head*, 1977]. Small, fresh craters formed into a smooth homogeneous target are more likely to have the smallest azimuthally varying topography than more degraded or larger craters and basins formed by impacting into the same target. A pre-impact surface that is not-flat and featureless but sloping or is already heavily cratered can have large effects on the final topography of an impact structure. Other sources of topographic variation include heterogeneous target layering, varying impact conditions (impactor composition, impact angle, etc.) [*Melosh*, 1989; *Schultz*, 1992a], and post-impact processes such as younger impacts, volcanism or tectonism [*Head*, 1975]. Determining the relative roles of these processes in modifying the final crater's topography has been a major goal of previous and current analyses.

[10] To account for these topographic variations, *Pike* [1976] averaged multiple elevation points to obtain a single statistic. For example, a single value for the rim-crest elevation was determined by first visually outlining the crater's rim crest, then sampling multiple elevation points along this outline, using more data points for the largest crater diameters. The floor elevation was also obtained from multiple spot elevations; the depth of the crater could then be calculated by subtracting this average floor elevation from the average rim-crest elevation. While providing the most accurate crater measurements at the time, this technique was highly limited by the number and quality of the LTOs, with far fewer topographic measurements available from shadow measurements of LO images. It is also unclear how many points were used for these calculations and what criteria were chosen for identifying the locations of the rim-crest and floor spot elevations.

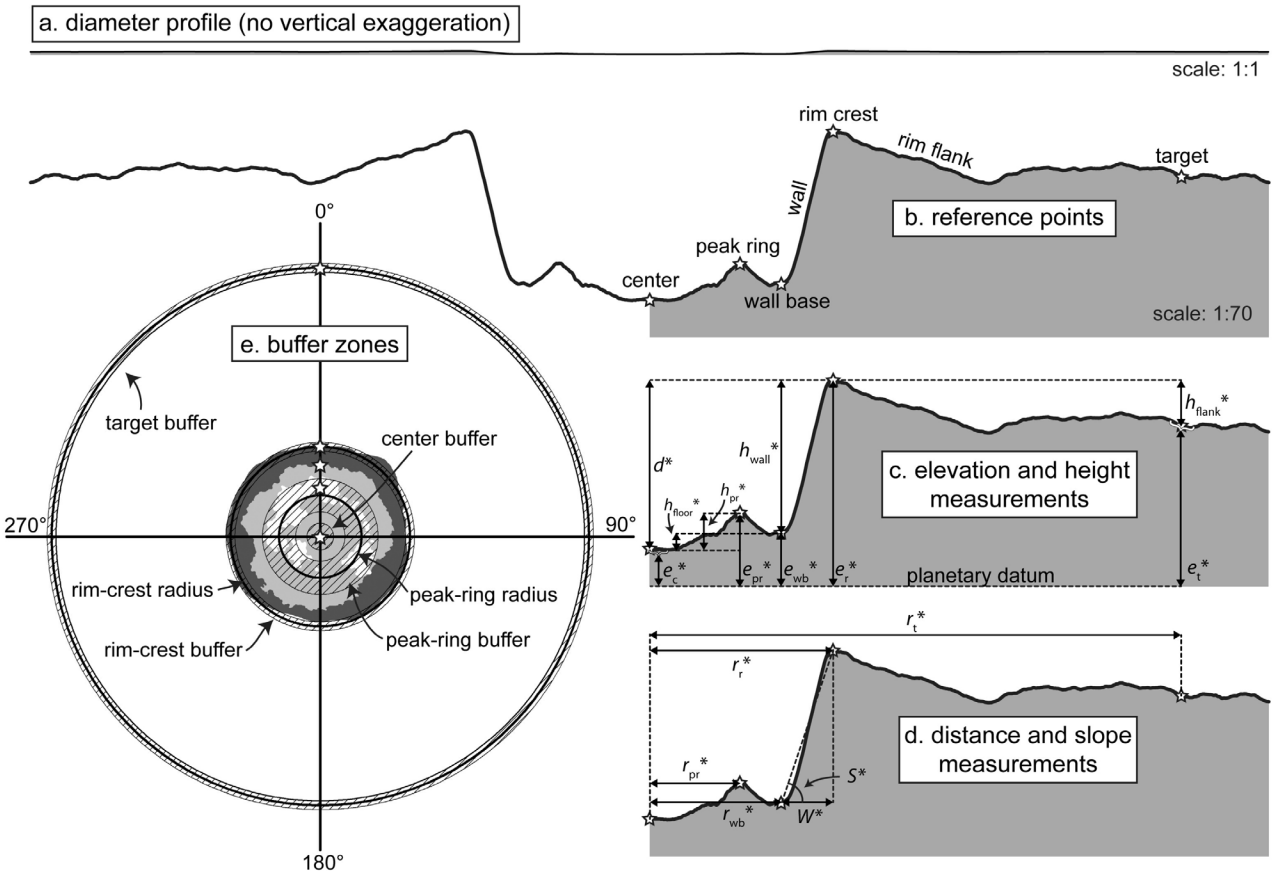

Figure 2. Location of measurements of the geometries of peak-ring basins in this study. A radially averaged profile of Schrödinger basin is used and is shown as a full diameter profile with (a) no vertical exaggeration and (b) ~70x vertical exaggeration. Topographic measurements use radial profiles starting from the center of the basin (Table 1) outward to a range of 3.5 times the basin radius. For the names of the abbreviations used in this figure, the reader is referred to the list of measured parameters in Table 2. The locations and names of the five reference points used to calculate geometries (center, peak ring, wall base, rim crest, and target) are shown in Figure 2b. The names of other major basin features are also included. (c) For each radial profile, elevations from planetary datum are measured for each reference point (e_c^*, e_{pr}^*, e_{wb}^*, e_r^*, e_t^*), from which a set of height calculations (d^*, h_{floor}^*, h_{pr}^*, h_{wall}^*, h_{flank}^*) can be made. (d) The radial distances to each reference point are also measured (r_{pr}^*, r_{wb}^*, r_r^*, r_t^*), from which wall width (W^*) is calculated for use in the wall slope (S^*) calculation. (e) Except for the wall base, the positions of reference points (Figure 2b) were located within a series of four buffer zones (center, peak-ring, rim-crest, and target buffers; dashed areas), defined as percentages of the rim-crest or peak-ring radii. Thick black lines show the locations of the measured rim-crest and peak-ring diameters from *Baker et al.* [2011a]. The background shows the outlines of the floor (light gray), peak-ring (white) and wall (dark gray) materials of Schrödinger basin for reference. For a description of how these buffer zones were determined, the reader is referred to section 4.2 of the text.

[11] *Williams and Zuber* [1998] examined the depths of large impact basins using Clementine lidar data. Like *Pike* [1976], they calculated a single value for the rim-crest elevation by taking an average of rim-crest elevations along the crater rim crest and subtracting an average floor elevation to obtain a basin depth. Again, these measurements suffered from the limitations of the topography data, as the ~60 km spacing between the Clementine lidar tracks greatly limited the number of data points available for determination of the elevations of the rim crest and floor. Initial geometric characterization of craters and basins using LOLA data have been made by several workers [e.g., *Kalynn et al.*, 2011; *Sori and Zuber*, 2011; *Talpe et al.*, 2011], however, a detailed procedure outlining techniques for calculating various geometric parameters from DEMs for basin-sized impact structures is currently lacking.

[12] To fully represent the topography of the original impact crater shape, a number of methodological criteria should be met. Ideally, calculations should include many data points over a complete range of azimuth, be systematic so that they can be readily reproduced by others, avoid subjective biases, avoid areas that have been obviously

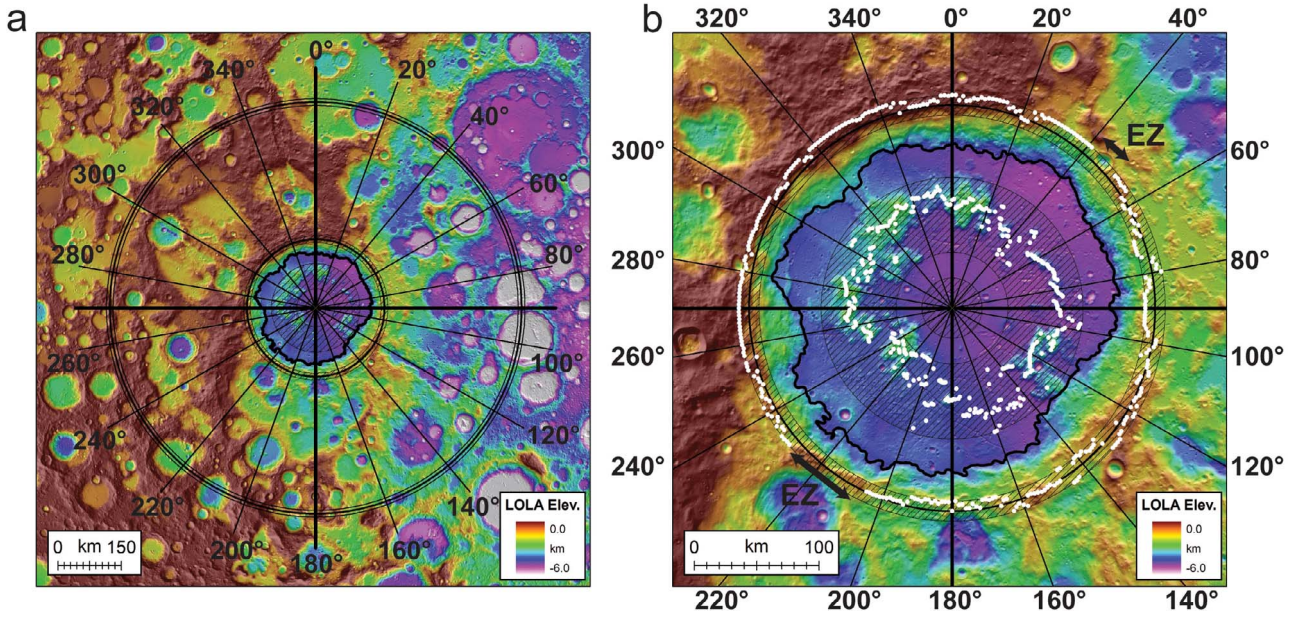

Figure 3. LOLA colored topography of Schrödinger basin (326 km, 74.90°S, 133.09°E) illustrating how reference points (Figure 2b) are located within pre-defined buffer zones. (a) Outlines of the four buffer zones (dashed areas; see also Figure 2e) and locations of the radial profiles given in Figure 4, which are separated by 20° of azimuth. The azimuth for due north is defined as 0°, with increasing azimuth occurring in the clockwise direction. (b) Close-up of Schrödinger basin showing the locations of the rim-crest and peak-ring reference points determined for each profile (1° azimuthal interval, white points) within each buffer zone. Azimuthal gaps in the reference points are due to pre-defined exclusion zones ("EZ"), where superposed impactor craters are disrupting the topography of Schrödinger basin. The irregular thick black outline defines the locations of the wall-base reference points.

affected by post-impact processes, and be robust with respect to the statistical techniques used for the calculation. With the current availability of high-resolution DEMs and the current level of computing power available for most personal computer workstations, it is now possible to meet these criteria with substantially higher fidelity. Considering these criteria, we now outline a new semi-automated procedure for extracting the geometric properties of impact basins on the Moon.

4. Improved Techniques for Calculating Geometric Properties of Impact Basins

[13] To improve the techniques for calculating impact basin geometries, we have automated the extraction of topographic information from DEMs along a set of radial topographic profiles extending from the center of a basin of interest outward to a specified range (Figures 2, 3, and 4). Each radial profile tracks a great circle path, which most accurately accounts for the curvature of the planetary surface at large basin sizes. Radial profiles are offset by a specified azimuth interval, which we set to 1° in all calculations to achieve statistically significant results. Thus, for a complete azimuthal range, 360 radial profiles for each basin are used for topographic calculations. However, superposed impact craters and other post-impact processes can significantly skew these calculations toward inaccurate values. We resolve this issue by defining "exclusion zones" (e.g., Figure 3) over azimuth ranges whereby no topographic information is to be extracted. These exclusion zones are mostly over areas substantially modified by superposed impact craters. Azimuth exclusion zones are defined for three "buffer zones" within the basin, including the rim-crest buffer, peak-ring buffer, and center buffer (see Figure 2 and section 4.2). The number of exclusion zones range from zero to nine over azimuthal intervals of typically between 5° to 70° of arc. As a result, the number of radial profiles for each basin may be reduced from a complete set of 360 to as few as 82 (average number of profiles within the rim buffer is 230; see Table 1).

[14] While high-resolution global LOLA DEMs down to 1024 ppd are now publically available to use, we chose to use 128 ppd (~236 m/pixel) gridded LOLA data for our topographic analysis, including all filtered shot data up to June 2011. The 128 ppd gridded data is sufficient for the scale of the features we are analyzing, while being computationally efficient for the software we used for our analysis. Our profile extraction program is written for MATLAB and uses the suite of tools provided in its Mapping Toolbox. Topographic profiles are extracted from the gridded DEM using bilinear interpolation at a point spacing set to mimic the resolution of the DEM (i.e., 128 ppd, or 236 m/pixel). While interpolating between the grid cells introduces some uncertainty in the topographic calculations, it is negligible given the basin's inherent topographic variation at the scales of the features we wish to characterize. More detailed, decameter-scale topographic characterization of a single basin should utilize higher-resolution DEMs or individual shot data to avoid inaccurate portrayal of topographic features.

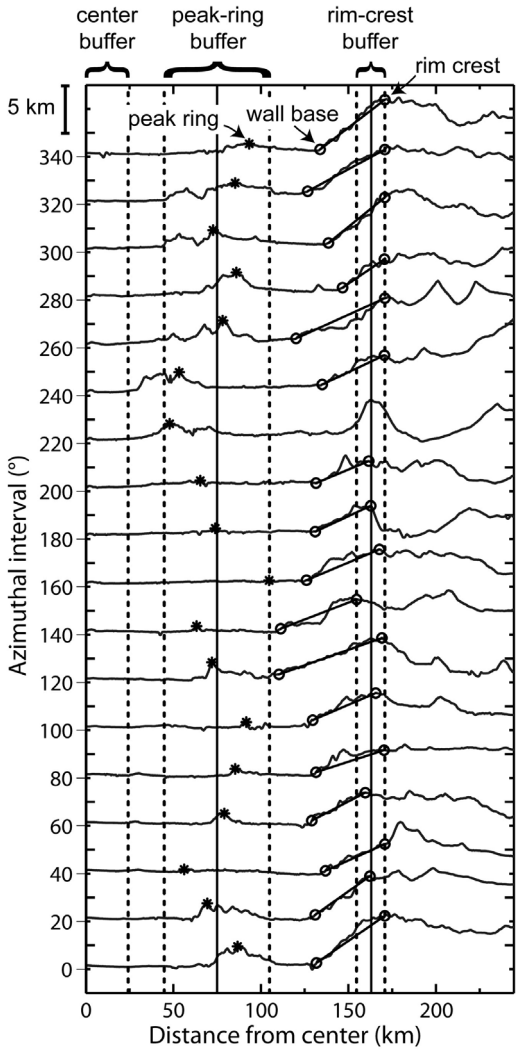

Figure 4. Radial topographic profiles at 20° azimuthal intervals for Schrödinger basin, shown out to 1.5 times the basin radius (244.5 km). The locations of each profile track are shown in Figure 3, with 0° azimuth defining north and increasing azimuth in the clockwise direction. The limits of the center, peak-ring, and rim-crest buffer zones (Figure 3a) are given as vertical dashed lines, with the location of the rim-crest diameter and ring diameter as measured by *Baker et al.* [2011a] given as solid vertical lines. Also shown are the locations of the peak-ring (asterisk, *), wall-base (open circle), and rim-crest (open circle) reference points determined within each buffer zone. The solid line connecting the wall-base and rim-crest reference points represent the reference line used to estimate the wall slope. No wall-base and rim-crest reference points are given for the profile at 220° azimuth, due to an exclusion zone over this interval (Figure 3b).

4.1. The Basin Catalog

[15] Peak-ring basins and protobasins under study are from the catalogs of *Baker et al.* [2011a], which include measurements of the basins' rim-crest, peak-ring, and central peak (for protobasins) diameters along with the central coordinates of a circle fit to the rim crest. To filter the most degraded basins from our topographic analysis, these basins of *Baker et al.* [2011a] were first qualitatively classified based on their degradation state on a scale of I to IV, with IV being the most degraded and I being the morphologically freshest basins (Table 1). These classifications were based on the number of superposed craters and the completeness and degree of erosion of the rim crest and walls. Only those basins with degradation classes of I or II were included in the analysis, which includes 8 of 17 peak-ring basins and 3 of 3 protobasins in the catalogs of *Baker et al.* [2011a] (Table 1).

[16] We also examined the general geology of the protobasins and peak-ring basins using LRO Wide-angle Camera (WAC) mosaics at 100 m/pixel resolution [*Robinson et al.*, 2010] and previous lunar geological maps [*Wilhelms and El-Baz*, 1977; *Lucchitta*, 1978; *Stuart-Alexander*, 1978; *Wilhelms et al.*, 1979], in order to identify possible effects of mare infill on the topography of basins. Three peak-ring basins (Schrödinger, Moscoviense, and Apollo) and two of the three protobasins (Antoniadi and Compton) have mare or mare-like material within their interiors [*Stuart-Alexander*, 1978; *Wilhelms et al.*, 1979; *Haruyama et al.*, 2009; *Mest et al.*, 2010]. Although some of the topographic characteristics of these basins, especially basin depths, have certainly been modified by this infilling, the preservation of prominent peak-ring topography and low areal extent of the mare material in most of the basins suggest that modification has been very limited compared to other mare-filled basins where peak rings and other interior landforms have been completely covered. For example, the most recent estimates for mare thicknesses in Mare Orientale in the Orientale basin, which also preserves much of its original topography, are on order of ~200 m [*Whitten et al.*, 2011], less than previous estimates [e.g., *Head*, 1982]. With the preservation of peak-ring topography and the smaller diameters of peak-ring basins and protobasins, it is unlikely that mare material thicknesses in these basins are much greater than a few hundred of meters. While mare infilling is certainly affecting our measurements, several hundred meters of mare fill is well below the already inherent kilometer-scale topographic variation in the rim-crest topography (see Figure 5). As such, we did not exclude those basins that have been partially infilled with mare from our topographic analysis. Two basins, Schrödinger and Compton, exhibit fracture patterns that crosscut all floor units and peak-ring material and bear resemblance to some floor-fractured craters [*Schultz*, 1976]. Based on the proposed mechanism for how floor fractures occur in these craters [*Schultz*, 1976], it is possible that Compton and Schrödinger could have experienced post-impact uplift of their floors that could modify our topographic calculations. Upon analysis of multiple topographic profiles across their floors, we find little evidence of doming that may have initiated fracturing of their interiors. However, it is noted that Compton appears to have an anomalously small depth compared to other protobasins (see section 5.1). While this may be a product of the floor-fracturing process, it may also represent an important geometric variation in the transition from complex craters to peak-ring basins or a product of varying impact conditions (see section 5.1). For these reasons, we therefore chose to include both Schrödinger and Compton in our analysis.

Table 1. List of Peak-Ring Basins and Protobasins Used in This Study, Which are From the Catalogs of *Baker et al.* [2011a][a]

Name	Latitude[b]	Longitude[b]	D_r	D_{pr}	D_{cp}	Class	Number of Profiles			Notes
							Rim Buffer	Ring Buffer	Center Buffer	
Peak-Ring Basins										
Schwarzschild	70.3554	120.0916	207	71	-	II	284	236	283	
D'Alembert	51.0543	164.8361	232	106	-	II	228	82	240	
Milne	−31.2532	112.7747	264	114	-	III	-	-	-	
Bailly	−67.1813	−68.7959	299	130	-	II	240	117	195	
Poincare	−57.3193	163.1533	312	175	-	IV	-	-	-	
Coulomb-Sarton	51.3494	−122.5339	316	159	-	IV	-	-	-	
Planck	−57.3913	135.0916	321	160	-	III	-	-	-	
Schrödinger	−74.9047	133.5332	326	150	-	I	327	360	360	mare
Mendeleev	5.4436	141.1357	331	144	-	II	243	118	303	
Birkhoff	58.8803	−146.5760	334	163	-	IV	-	-	-	
Lorentz	34.2963	−96.9955	351	173	-	IV	-	-	-	
Schiller-Zucchius	−55.7155	−45.1765	361	179	-	IV	-	-	-	
Korolev	−4.4430	−157.4701	417	206	-	II	219	173	124	
Moscoviense	26.3355	147.3612	421	192	-	I	241	126	297	mare
Grimaldi	−5.0105	−68.6893	460	234	-	IV	-	-	-	
Apollo	−36.0934	−151.4845	492	247	-	II	192	114	272	mare
Freundlich-Sharonov	18.3493	175.0039	582	318	-	IV	-	-	-	
Protobasins										
Antoniadi	−69.3530	−172.9644	137	56	6	I	360	234	360	mare
Compton	55.9219	103.9596	166	73	15	I	360	288	360	mare
Hausen	−65.3381	−88.7572	170	55	31	I	352	243	233	

[a]Given are the measured diameters (in kilometers) of the rim crest (D_r), peak ring (D_{pr}), and central peak (D_{cp}) (for protobasins) and the center coordinates for each basin, as determined by *Baker et al.* [2011a]. The degradation class for each basin is listed, as well as the number of profiles used within each buffer for determining the profile and basin statistics. Only those basins with degradation classes of I or II were used in our analysis. We also note those basins with mapped mare deposits.

[b]Latitudes are positive northward and negative southward. Longitudes are positive eastward and negative westward.

4.2. Individual Profile Statistics

[17] All radial profiles started at the basin's center coordinates as defined by *Baker et al.* [2011a] (Table 1). These center coordinates correspond to the centroid of a circle fit to the basin's rim crest and are assumed to best represent the basin center without any a posteriori information obtained from subsequent calculations. We then specified the range of each profile, the azimuthal interval and any "exclusion zones." All profiles were set to a range of 3.5 times the rim-crest radius as measured by *Baker et al.* [2011a]. As mentioned above, topographic profiles were offset by 1° azimuth intervals and were not extracted over pre-defined "exclusion zones" within each of the three buffer zones (Figure 2).

[18] For each profile, we defined the locations and elevations of five reference points for use in subsequent calculations, including the center, peak ring, wall base, rim crest and target (Figure 2 and Tables 2 and 3). These reference points were selected to calculate the main topographic properties traditionally used in the topographic characterization of craters [*Pike*, 1976] (Figure 1). All reference points, except for the wall base and the distance to the target reference point, were located within pre-defined buffer zones (Figure 2), set as percentages of the measured rim-crest and peak-ring diameters from *Baker et al.* [2011a] (Table 1). These buffer zones were included to account for the uncertainties in locating maximum rim-crest and peak-ring elevations along the profile and also to reduce the statistical effect of extreme local topographic variations.

[19] The rim-crest buffer was set to ±5% of the rim-crest radius, which corresponds to the estimated error in the rim-crest diameter measurements of *Baker et al.* [2011a]. The rim-crest reference point was then defined as the maximum elevation point within the rim-crest buffer (Figures 2b, 3, and 4). The peak-ring buffer was set to ±30–40% of the peak-ring radius, which accounts for uncertainly in the measurement of peak-ring diameter and the significant offset that occurs between the centroid of a circle fit to the basin's peak ring and rim crest (see section 5.6 and Table 6). The peak-ring reference point was then defined as the maximum elevation point within the peak-ring buffer (Figure 3b and 4). A center buffer was also set, starting from the basin's center coordinates to 15% of the rim-crest radius, which was found to be a reasonable distance for obtaining a statistically representative center elevation without incorporating peak-ring material in the measurement. For protobasins, which have a central peak, the center buffer was modified to extend from a distance equal to two times the radius of the central peak (Table 1) to the lower limit of the peak-ring buffer. The target buffer was set to ±5% of the rim-crest radius to smooth out the effects of simple craters (<20 km in diameter) falling within the target buffer. Elevations for the center and target reference points were calculated as the median of all elevation points within the buffers, with uncertainties calculated as the interquartile range of these elevation points (Table 2). The distance to the target reference point was set to 3 basin radii from the center reference point (Table 3). This value is about one crater radius beyond the estimated ejecta width determined by *Pike* [1977] and should therefore be dominated by the topography of the pre-impact target surface. However, the pre-impact topography has been highly affected by superposed impact craters, making accurate determination of the elevation of the target reference point difficult (section 5.2). No buffers were set for determining the elevation and distance to the wall-base reference point due to the difficulty in

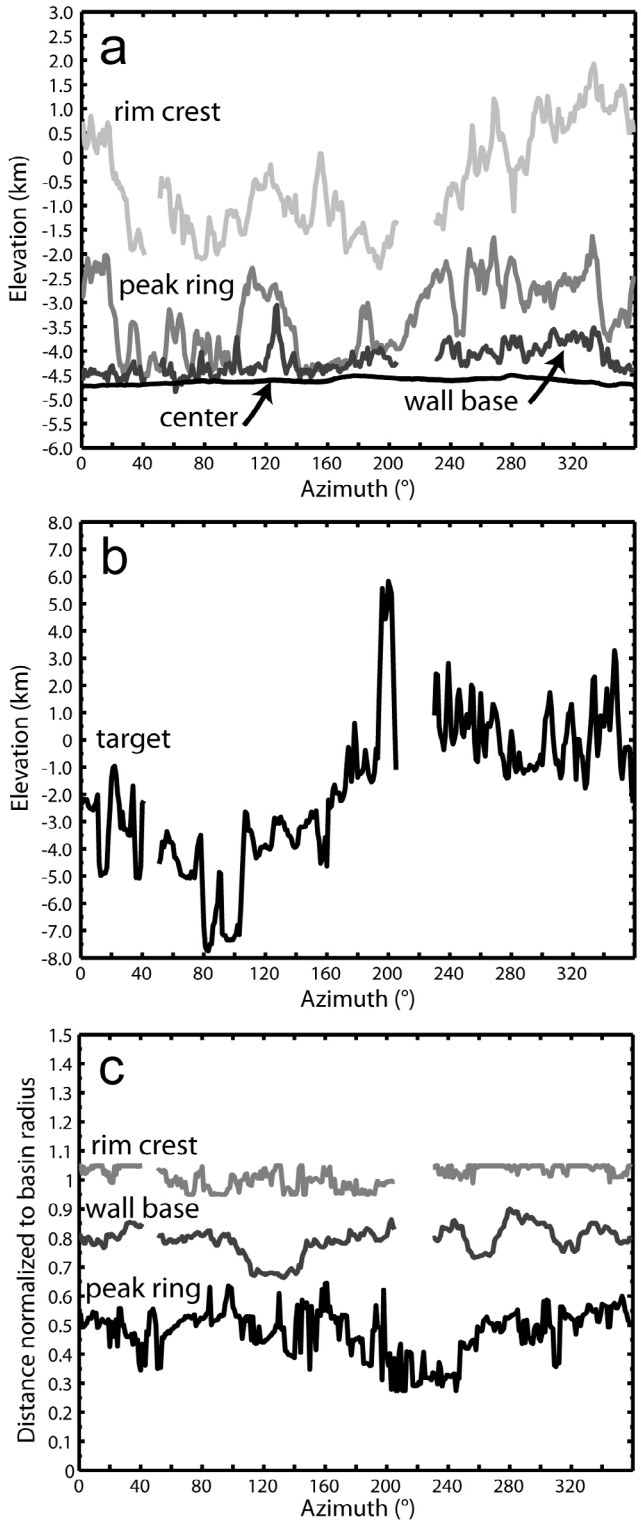

Figure 5. Variation in the elevations and distances of reference points with azimuth for Schrödinger basin. (a) Elevation of the rim-crest, peak-ring, wall-base, and center reference points as a function of azimuth. (b) Elevation of the target reference point as a function of azimuth. (c) Distances to the rim-crest, wall-base, and peak-ring reference points normalized to the rim-crest radius of Schrödinger (163 km).

automating the process for locating this reference point in topographic profiles. Instead, we first manually digitized the locations of the wall base as a polygon using LOLA hillshade and color gridded topography (Figure 3b). The location of the wall base is therefore a topographic feature, representing the break in slope between the base of the basin wall and the floor (Figure 3b and 4). Although this is our best approximation of the location of the wall base from LOLA data, burial of the toes of wall slump blocks by impact melt or basin infill material, such as ejecta, may obscure the exact location of the wall base [*Settle and Head*, 1979]. Elevations at the digitized wall-base locations were then extracted from the LOLA DEM for each profile.

[20] After determining the elevation and distance values for the five reference points (center, peak ring, wall base, rim crest, and target), a number of derived parameters were then calculated for each profile (Table 2). To distinguish these derived parameters calculated for an individual profile from the final basin summary statistics (see section 4.4 below), we denote calculated parameters determined from a single profile with an asterisk (*) (Table 2). Distances we calculated for each profile include the wall width (W^*) (Figure 2d). Heights we calculated include the basin depth (d^*), peak-ring height (h^*_{pr}), floor height (h^*_{floor}), wall height (h^*_{wall}), and rim-flank height (h^*_{flank}) (Figure 2c). Further calculations include the slope of the rim wall (S^*) (Figure 2c), which was calculated as the inverse tangent of the wall height divided by the wall width. A summary of the abbreviations and formulas used for calculating these derived parameters is given in Table 2.

4.3. Azimuthal Variation and Location Statistics

[21] For each basin, up to 360 individual profiles were produced, yielding azimuthally changing distance, elevation, and slope measurements. Figure 4 shows a subsample of the topographic profiles taken at 20 degree azimuthal intervals for Schrödinger basin. As observed from these profiles, the locations of the rim-crest, peak-ring, and wall-base reference points are highly variable between profiles. This is better illustrated if we plot the elevations and distances of the reference points as a function of azimuth over 1° intervals (Figures 5 and 6). As shown, there is upwards of 3–4 km in topographic variation for the elevations of the rim crest, with a ~2 km range in elevation of the peak ring. The wall-base and center elevations are the least varying reference points (Figure 5a), with only a few tens to hundreds of meters of topographic variation. The elevation of the target reference point is the most varying of the reference points (Figure 5b), having a maximum range of >10 km. Most of this variation is due to the effects of impact craters within the target buffer (Figure 3a), which are unavoidable when trying to measure a pre-impact surface for impact structures as large as peak-ring basins. The distances to the reference points also change considerably with azimuth (Figure 5c). The distance to the peak ring is highly variable due to the inherent disaggregated character of peak rings and also due to the fact that the centroids of most peak rings are offset from the centroids of the rim crest (section 5.6).

[22] The variations in distances and elevations of the reference points are also propagated to the derived parameters calculated for each profile (i.e., W^*, d^*, h^*_{pr}, h^*_{wall}, h^*_{flank}, and S^*) (Figure 6). For example, since the elevation of the

Table 2. List of the Names, Abbreviations, and Formulas Used in Determining Basin Geometries[a]

	Statistics per Profile		Statistics per Basin	
	Abbreviation	Formula[b]	Abbreviation	Formula[b]
		Elevations		
Center	e_c^*	Q2{bc_1… bc_m}	e_c	Q2{$bc_{1,1}$… $bc_{m,n}$}
Peak ring	e_{pr}^*	-	e_{pr}	Q2{$e_{pr,1}^*$… $e_{pr,n}^*$}
Wall base	e_{wb}^*	-	e_{wb}	Q2{$e_{wb,1}^*$… $e_{wb,n}^*$}
Rim crest	e_r^*	-	e_r	Q2{$e_{r,1}^*$… $e_{r,n}^*$}
Target	e_t^*	Q2{bt_1… bt_m}	e_t	Q2{$bt_{1,1}$… $bt_{m,n}$}
		Radial Distances		
Center	r_c^*	-	r_c	-
Peak ring	r_{pr}^*	-	r_{pr}	Q2{$r_{pr,1}^*$ … $r_{pr,n}^*$}
Wall base	r_{wb}^*	-	r_{wb}	Q2{$r_{wb,1}^*$ … $r_{wb,n}^*$}
Rim crest	r_r^*	-	r_r	Q2{$r_{r,1}^*$ … $r_{r,n}^*$}
Target	r_t^*	-	r_t	r_t^*
		Derived Parameters		
Wall width	W^*	$r_r^* - r_{wb}^*$	W	Q2{W_1^* … W_n^*}
Peak-ring height	h_{pr}^*	$e_{pr}^* - e_c^*$	h_{pr}	$e_{pr} - e_c$
Floor height	h_{floor}^*	$e_{wb}^* - e_c^*$	h_{floor}	$e_{wb} - e_c$
Wall height	h_{wall}^*	$e_r^* - e_{wb}^*$	h_{wall}	Q2{$h_{wall,1}^*$… $h_{wall,n}^*$}
Depth	d^*	$e_r^* - e_c^*$	d	$e_r - e_c$
Rim-flank height	h_{flank}^*	$e_r^* - e_t^*$	h_{flank}	Q2{$h_{flank,1}^*$… $h_{flank,n}^*$}
Wall slope	S^*	$\tan^{-1}(h_{wall}^*/W^*)$	S	Q2{S_1^*… S_n^*}
Volume	not calculated	not calculated	V_1	(see equation (1))

[a]Parameters in the left columns are those calculated for each profile and are denoted by an asterisk (*). Parameters in the right columns are those calculated for a single basin using all profiles. A diagram illustrating the locations of these measurements on the peak-ring basin profile is given in Figure 2.

[b]Q2{…} denotes calculation of the second quartile statistic (i.e., the median), n is the number of profiles per basin, and m is the m^{th} point within the center buffer (*bc*) or target buffer (*bt*).

center does not vary substantially with azimuth (Figure 5a), the calculation for basin depth (d^*) is essentially determined by the elevation of the rim crest, resulting in a ~3 km range in depth measurements for Schrödinger (Figure 6a). In a similar fashion, the variation in height of the rim flank (h_{flank}^*) (Figure 6b) is mostly controlled by the reference point with the largest varying topography, which is the elevation of the target (Figure 5b). Wall height (W^*) varies by as much as 40 km (Figure 6c), with wall slope (S^*) varying as much as 7° (Figure 6d).

[23] How do we account for these substantial azimuthal variations in topography when calculating a single summary statistic such as basin depth? While we have improved our sample size by systematically sampling elevations and distances over a much larger azimuthal range than previous studies, we are also capturing a much larger range of topographic variation. As mentioned, *Pike* [1976] accounted for some of the variation in the rim-crest topography by taking the mean elevation of a series of points along an outline of the rim crest. *Williams and Zuber* [1998] applied a similar technique in their calculation of basin depth. Is using the mean value the most representative statistic for calculating basin geometries? To address this question, we qualitatively examined the distributions of the derived parameters calculated for each radial profile for each peak-ring basin. Using Schrödinger as an example, we see that the distributions are generally non-normal and commonly have long tails and are sometimes bimodal or more uniformly distributed (Figure 7). Use of the mean statistic would skew the calculation toward any tails (extrema) in the distribution, which would misrepresent the central tendency of the sample set. A more robust statistic with respect to extrema in the sample set would be to use the median value. Use of this statistic also allows the variation in topography to be represented by the interquartile range (i.e., the middle 50% of the population about the median value), which measures the spread of the sample set close to the median value without being largely affected by extrema. Considering the robustness of use of the median statistic, we chose to use this exclusively when calculating the statistics for peak-ring basins and protobasins in this study. For perfectly normal distributions, the mean and median values are the same. Some of the measured parameters, however, take on more uniform or bimodal distributions, in which case neither the mean nor the median are useful measures of location. For simplicity, we still use the median and interquartile range for these more complex distributions.

4.4. Basin Summary Statistics

[24] From the set of individual profile measurements, elevations and distances of reference points for the entire basin were calculated (Tables 2 and 3). These values are different from those calculated for individual profiles, as all radial profiles are used in the calculation of the statistics for a single basin. Following the discussion in the previous section, the peak-ring, wall-base, and rim-crest elevations (e_{pr}, e_{floor}, e_r) and distances (r_{pr}, r_{floor}, r_r) were defined as the median value of the set of reference points from all topographic profiles (e.g., Q2{$e_{pr,1}^*$…$e_{pr,n}^*$}, where n is the number of profiles and Q2{} represents the calculation of the second quartile statistic (i.e., the median) of the set of values) (Tables 2 and 3); the interquartile range of these sets of reference points represent the azimuthal variation. The

Table 3. The Distances and Elevations Determined for the Center, Peak-Ring, Wall-Base, Rim-Crest, and Target Reference Points (Figure 2) for Each Basin[a]

Name	Radial Distances (km)					Elevations (km)				
	r_c	r_{pr}	r_{wb}	r_r	r_t	e_c	e_{pr}	e_{wb}	e_r	e_t
Peak-Ring Basins										
Schwarzschild	0	26.41 (+8.41, −2.96)	80.19 (+5.33, −6.99)	107.67 (+0.83, −3.79)	310.54	−3.46 (+0.12, −0.04)	−2.84 (+0.35, −0.28)	−3.27 (+0.10, −0.07)	−0.45 (+0.54, −0.74)	−1.32 (+0.72, −0.97)
D'Alembert	0	52.12 (+1.66, −4.26)	91.21 (+4.74, −2.96)	120.35 (+1.18, −2.13)	347.54	−1.42 (+0.07, −0.08)	−1.00 (+0.11, −0.17)	−0.77 (+0.07, −0.09)	3.18 (+0.33, −0.44)	1.29 (+0.76, −0.77)
Bailly	0	72.02 (+6.46, −8.77)	121.53 (+10.07, −6.87)	154.34 (+2.49, −3.91)	449.04	−1.50 (+0.20, −0.12)	−0.37 (+0.27, −0.29)	−0.82 (+0.15, −0.19)	2.64 (+0.67, −0.90)	−1.14 (+1.55, −0.96)
Schrödinger	0	80.90 (+5.45, −9.59)	129.82 (+4.74, −3.55)	166.54 (+4.26, −4.97)	488.75	−4.61 (+0.05, −0.04)	−3.27 (+0.64, −0.73)	−4.27 (+0.29, −0.15)	−0.63 (+1.07, −0.76)	−1.65 (+1.56, −2.01)
Mendeleev	0	63.84 (+6.04, −5.57)	124.14 (+2.78, −2.78)	167.02 (+5.39, −5.21)	496.19	−1.15 (+0.04, −0.02)	−0.34 (+0.48, −0.43)	−0.88 (+0.26, −0.18)	4.39 (+0.74, −0.53)	1.80 (+1.09, −1.03)
Korolev	0	103.29 (+11.90, −15.40)	172.23 (+5.21, −5.21)	217.71 (+0.95, −4.20)	625.71	2.65 (+0.12, −0.06)	4.07 (+0.53, −0.82)	3.31 (+0.48, −0.21)	7.35 (+0.53, −0.58)	3.58 (+1.46, −1.45)
Moscoviense	0	112.41 (+9.36, −14.81)	164.65 (+3.08, −4.50)	214.16 (+4.74, −6.46)	631.68	−3.28 (+0.04, −0.02)	0.45 (+0.76, −0.75)	−1.68 (+0.48, −0.81)	3.13 (+0.45, −0.49)	0.83 (+1.30, −0.99)
Apollo	0	125.20 (+14.33, −19.07)	208.12 (+15.40, −7.58)	255.97 (+2.01, −6.51)	738.09	−5.47 (+0.01, −0.03)	−2.55 (+0.46, −0.55)	−4.20 (+0.29, −0.74)	−0.71 (+1.00, −2.33)	−0.12 (+3.33, −4.70)
Protobasins										
Antoniadi	0	27.36 (+4.62, −1.54)	51.17 (+3.55, −3.55)	69.89 (+1.42, −1.18)	205.56	−7.35 (+0.01, −0.01)	−6.70 (+0.63, −0.35)	−6.73 (+0.09, −0.13)	−3.25 (+0.42, −0.42)	−4.71 (+0.57, −0.66)
Compton	0	36.13 (+6.16, −7.94)	61.00 (+2.72, −5.09)	84.34 (+2.61, −3.32)	249.17	−3.38 (+0.08, −0.06)	−3.14 (+0.16, −0.08)	−3.29 (+0.07, −0.06)	−0.98 (+0.77, −0.44)	−1.58 (+0.74, −1.16)
Hausen	0	31.51 (+5.15, −4.50)	54.01 (+3.32, −3.79)	85.76 (+2.61, −3.20)	254.80	−1.20 (+0.05, −0.05)	−0.93 (+0.09, −0.06)	−0.67 (+0.15, −0.08)	4.73 (+0.41, −0.55)	0.42 (+1.13, −1.79)

[a]The numbers in parentheses given for each parameter are the interquartile range for each parameter. No interquartile ranges are given for the radial distance to the target point (r_t), as this distance was set as 3 times the basin's rim-crest radius.

elevations of the center and target surface reference points (e_c and e_t) were calculated as the median and interquartile range of all elevation points within the center and target buffers for every profile (e.g., e_c = Q2$\{bc_{1,1}, \ldots, bc_{m,n}\}$, where *bc* denotes the center buffer, *m* is the m^{th} elevation point within the buffer, and *n* is the number of profiles) (Table 2 and 3).

[25] Derived parameters (i.e., heights, widths, slopes and volumes; see Table 4) for each basin were then calculated in two ways: 1) directly from the median and interquartile ranges of the basin summary reference points (e.g., $h_{pr} = e_{pr} - e_c$) and 2) by determining the median and interquartile range of the set of derived values already calculated for each profile (e.g., W = Q2$\{W_1^* \ldots, W_n^*\}$) (Table 2). We calculated the peak-ring height, floor height, and basin depth using the first method for consistency with previous studies that calculated heights as the difference between the mean elevations of features [*Pike*, 1974; *Williams and Zuber*, 1998]. Use of this method also maximized the number of profiles used in the calculations, as heights require that the center and peak-ring or rim-crest buffer zones do not have overlapping exclusion zones. Wall width, slope, and all distances were calculated using the second method to account for any azimuthal dependence on the calculations of these parameters. For a summary of all abbreviations and formulas used to calculate these statistics, the reader is referred to Table 2.

[26] We also calculated the volume of each basin in two ways. The first involved calculating the volume of a double frustum (V_1) using the radii of the rim crest and floor (r_r and r_{floor}), the center buffer radius (C), and basin depth and wall height (d and h_{wall}) (Table 4). The equation of the double frustum is:

$$V_1 = \pi/3\left[\left(r_r + r_r r_{floor} + {r_{floor}}^2\right)d + \left({r_{floor}}^2 + r_{floor}C + C^2\right)\left(h_{floor}\right)\right] \quad (1)$$

[27] The second method uses a volume calculation tool available from the geographical information system (GIS) software, ArcGIS. First, a polygon defining the extent of the basin interior was digitized using the set of rim-crest reference points for each basin. Then, the volume was calculated (V_2; see Table 4) as the integrated cubic distance between the surface of the polygon and facets of a 128 ppd LOLA DEM-derived Triangulated Irregular Network (TIN). The height of the polygon surface was set to the median and interquartile range of the elevations of the rim-crest reference points (Table 3), resulting in a median value for the volume with uncertainties (Table 4). We found that both methods provided consistent results, with percent differences of generally <10% and no obvious systematic differences (Table 4).

4.5. Effects of Regional Slope

[28] Previous authors have noted that regional slope can have substantial effects on the measured topography of craters, especially at the large scales of peak-ring basins and multi-ring basins [*Pike*, 1976; *Williams and Zuber*, 1998]. To determine how this might have an effect on our calculations, we ran our automated procedure incorporating a correction for regional slope (Figure 8). Our correction procedure involved fitting a line to pairs of complementary radial profiles (i.e., a full diameter profile) to obtain slopes

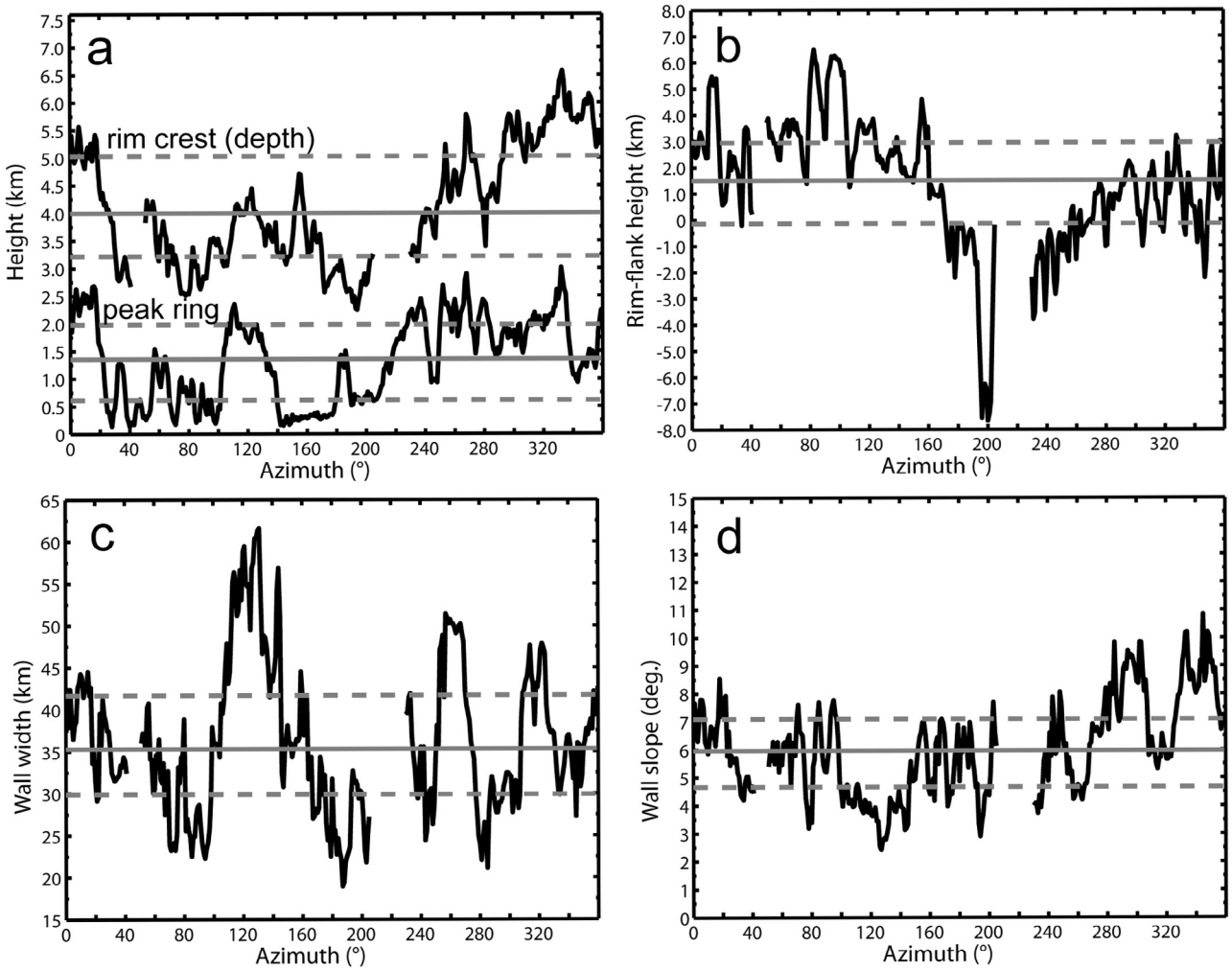

Figure 6. Variations in calculated heights, distances and slopes with azimuth for Schrödinger basin. The gray horizontal lines in each panel give the calculated median value for the parameter over the entire range of azimuth (solid line) and the interquartile range (dashed lines). These median values are used as the summary statistics for each basin (Table 4). (a) Height of the rim crest (i.e., basin depth) and height of the peak ring as a function of azimuth. Most of the variations in these parameters result from the highly variable nature of the rim-crest and peak-ring elevations (Figure 5). (b) Height of the rim flank as a function of azimuth. Most of the variation in this parameter is the result of the highly variable elevation of the target reference point. (c) Width of the wall as a function of azimuth. (d) Wall slope as a function of azimuth.

that were then leveled to create corrected profiles for use is calculating the elevation and distance values of the reference points and derived parameters. While this technique appeared to work well in leveling profiles in the presence of true, pre-impact regional slopes (Figure 8), percent differences between the corrected and uncorrected basin summary statistics were, on average, less than 10% for all peak-ring basins. Furthermore, our correction procedure did not account for the effects of younger basins that have substantially modified the terrain adjacent to some peak-ring basins (e.g., Figure 3a). These large, relatively younger basins form regional slope profiles that may be mistaken for pre-impact terrain in the automated correction procedure, leading to unnecessary regional slope corrections. Due to the small differences between the corrected and uncorrected data and the uncertainties of the correction resulting from the effects of nearby, younger basins, we chose to report only uncorrected data (Tables 3 and 4). Future automated corrections for regional slope should seek to improve upon the techniques described here.

5. Results

[29] Using our improved techniques for extracting the topography of impact basins from DEMs, we have calculated a number of summary statistics (Tables 4 and 5) that provide useful tools for evaluating the geometric properties of impact structures, as they constrain impact processes. As has traditionally been done, we plot these parameters as a function of the basins' rim-crest diameters, as measured by *Baker et al.* [2011a] (Table 1), and, except where indicated, plot these parameters in log-log space [*Baldwin*, 1949; *Pike*,

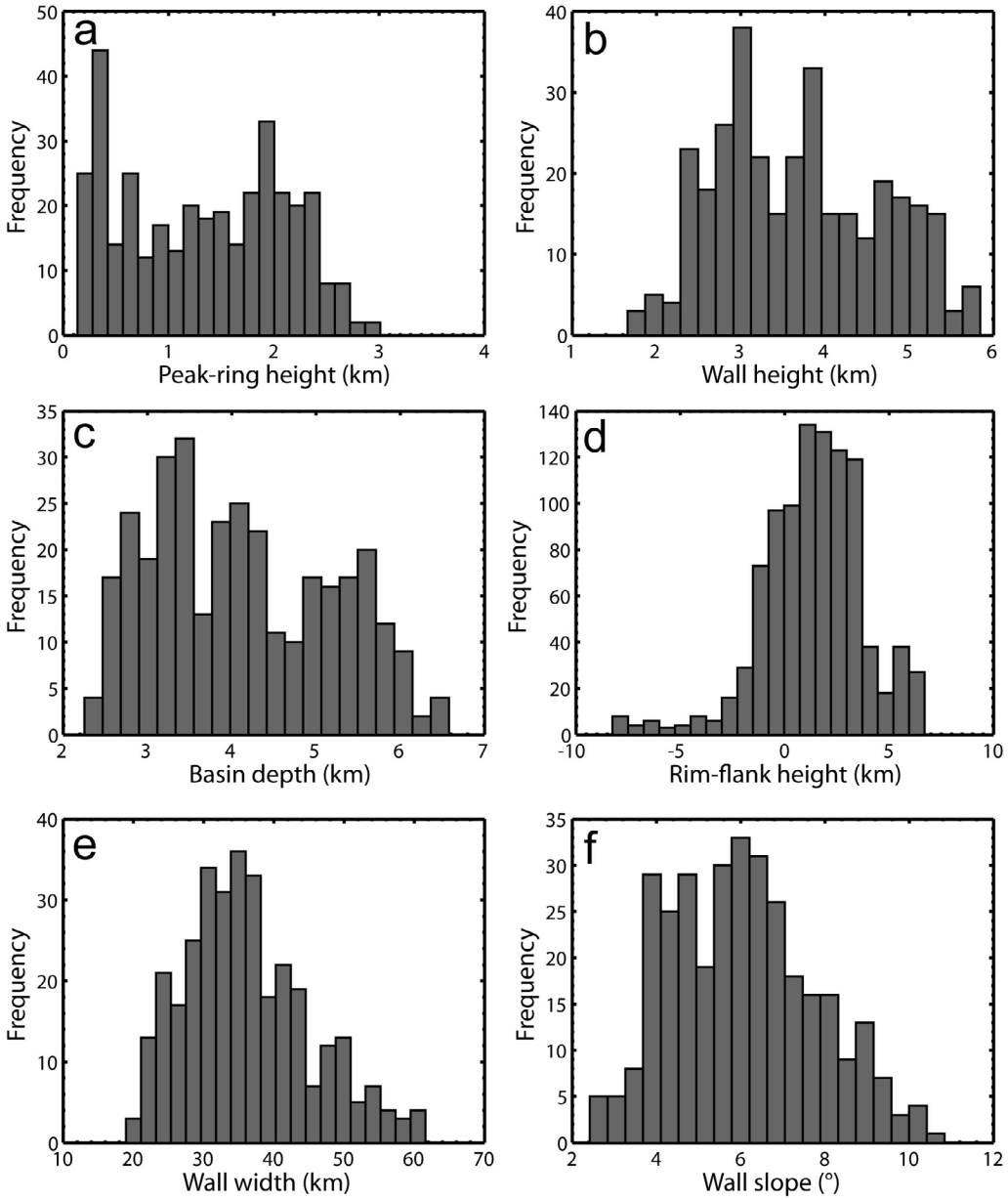

Figure 7. Histograms of calculated parameters over all azimuths for Schrödinger basin. The values are not normally distributed and commonly have long tails and wide distributions, indicating that use of the mean statistic is not a robust location parameter of the sample set.

1977] (Figure 9). All parameters are plotted as median values for reasons discussed in section 3 and shown in Table 2. Error bars in Figure 9 are the interquartile range for each median value and are used to represent the range of topographic variations as a function of azimuth around the crater (e.g., Figures 5 and 6). We also calculated a number of ratios from the median values of the summary statistics (Table 5). Due to the highly variable nature of the parameters used to calculate these ratios (i.e., large interquartile ranges), the error bars for the ratios can be very large and often distract from the trends revealed by the median values of these parameters. For clarity, we therefore chose to omit error bars from the plots of ratios (Figure 10). We also include qualitative trendlines in Figures 9 and 10 to facilitate discussion of our interpretations. Quantitative fits to the data are unwarranted due to the small sample size of the data and inherently variable nature of basin topography, which create large uncertainties during the fitting procedure. Despite these uncertainties, many new trends are observed (Figures 9 and 10), which extend the well-defined geometric trends for simple and complex craters out to basin-sized structures.

5.1. Basin Depth (*d*)

[30] Perhaps the most important and widely examined geometric parameter in crater morphological studies is the crater depth. While the trend of depth with increasing crater diameter is well characterized for simple and complex craters [*Pike*, 1974, 1977], the depths of larger basins on the Moon are poorly defined. *Williams and Zuber* [1998] (herein referred to

Table 4. Parameters Calculated From the Reference Points in Table 3[a]

Name	D_r	Derived Parameters									
		d	h_{floor}	h_{pr}	h_{wall}	h_{flank}	W	S (°)	V_1 (km^3)	V_2 (km^3)
Peak-Ring Basins										
Schwarzschild	207	3.01(+0.58, −0.85)	0.20 (+0.14, −0.19)	0.63 (+0.39, −0.39)	2.68 (+0.66, −0.63)	0.73 (+1.37, −0.89)	26.65 (+4.03, −5.92)	6.33 (+2.12, −1.28)	0.80 (+0.17, −0.22) × 10^5	0.81 (+0.19, −0.24) × 10^5
D'Alembert	232	4.60 (+0.41, −0.51)	0.65 (+0.15, −0.16)	0.42 (+0.19, −0.25)	3.94 (+0.37, −0.40)	1.78 (+1.02, −0.58)	28.55 (+3.55, −4.86)	7.87 (+0.98, −0.92)	1.45 (+0.19, −0.17) × 10^5	1.50 (+0.14, −0.19) × 10^5
Bailly	299	4.13 (+0.79, −1.10)	0.68 (+0.27, −0.40)	1.13 (+0.39, −0.49)	3.46 (+0.91, −0.98)	3.38 (+1.55, −1.28)	30.44 (+8.05, −9.83)	6.38 (+1.84, −0.97)	2.18 (+0.57, −0.50) × 10^5	2.33 (+0.47, −0.61) × 10^5
Schrödinger	326	3.98 (+1.12, −0.80)	0.35 (+0.33, −0.19)	1.34 (+0.69, −0.78)	3.61 (+0.89, −0.69)	1.50 (+1.44, −1.65)	35.30 (+6.40, −5.39)	5.96 (+1.13, −1.30)	2.58 (+0.90, −0.47) × 10^5	2.47 (+0.60, −0.45) × 10^5
Mendeleev	331	5.54 (+0.77, −0.57)	0.26 (+0.28, −0.22)	0.80 (+0.51, −0.47)	5.23 (+0.57, −0.52)	2.43 (+1.18, −0.81)	42.88 (+4.44, −4.50)	6.92 (+1.23, −0.92)	3.58 (+0.77, −0.45) × 10^5	3.63 (+0.62, −0.43) × 10^5
Korolev	417	4.70 (+0.59, −0.70)	0.66 (+0.54, −0.33)	1.42 (+0.59, −0.93)	3.91 (+0.43, −0.53)	3.57 (+1.68, −1.24)	42.88 (+6.10, −3.79)	5.19 (+0.62, −0.65)	5.06 (+0.85, −0.97) × 10^5	5.02 (+0.73, −0.79) × 10^5
Moscoviense	421	6.40 (+0.47, −0.54)	1.60 (+0.50, −0.85)	3.73 (+0.78, −0.79)	4.79 (+0.74, −0.62)	2.06 (+1.13, −1.16)	49.99 (+4.50, −6.16)	5.58 (+1.07, −0.74)	5.90 (+1.57, −0.99) × 10^5	5.76 (+0.60, −0.66) × 10^5
Apollo	492	4.77 (+1.03, −2.34)	1.28 (+0.32, −0.76)	2.93 (+0.50, −0.56)	3.33 (+1.04, −1.30)	−0.58 (+2.26, −1.92)	42.29 (+11.13, −14.57)	4.51 (+0.99, −1.01)	6.50 (+2.49, −3.03) × 10^5	6.81 (+1.87, −4.09) × 10^5
Protobasins										
Antoniadi	137	4.09 (+0.42, −0.42)	0.62 (+0.10, −0.13)	0.64 (+0.63, −0.36)	3.49 (+0.36, −0.37)	1.64 (+0.46, −0.94)	18.95 (+3.08, −3.32)	10.67 (+1.77, −1.53)	4.20 (+0.90, −0.65) × 10^4	4.56 (+0.62, −0.62) × 10^4
Compton	166	2.40 (+0.84, −0.52)	0.10 (+0.13, −0.14)	0.24 (+0.23, −0.16)	2.35 (+0.71, −0.48)	0.67 (+1.54, −0.69)	22.98 (+3.32, −3.32)	5.98 (+1.15, −0.97)	3.90 (+1.47, −0.75) × 10^4	3.74 (+1.64, −0.89) × 10^4
Hausen	170	5.93 (+0.46, −0.60)	0.53 (+0.20, −0.14)	0.28 (+0.14, −0.11)	5.35(+0.37, −0.57)	4.06 (+2.00, −0.84)	30.80 (+4.50, −3.08)	9.37 (+1.35, −1.04)	8.59 (+1.56, −1.51) × 10^4	9.02 (+0.92, −1.21) × 10^4

[a]All values are in kilometers except where denoted. Formulas for calculating these parameters are given in Table 2. The numbers in parentheses given for each parameter are the interquartile range for each parameter.

as *WZ*98) have provided the most comprehensive catalog of basin depths, but the accuracy of these measurements were limited by the quality of the Clementine lidar data and did not completely account for the substantial azimuthal variation in topography. *WZ*98 used individual orbital tracks from the Clementine lidar instrument and determined the depth as the difference between the center elevation, determined from all tracks crossing the central portion of the basin, and the rim-crest elevation, taken as the mean of all rim-crest elevations from each orbital track. Large uncertainties in these measurements are introduced from the limited number of orbital tracks crossing each basin and the coarse spacing between individual data points. *WZ*98 also used the mean values of rim-crest elevations, which is not a robust location parameter considering the non-normal distributions of the sample set (Figure 7 and section 3). As a result of these differences in methodologies and data sets, our median depth measurements (Table 4) have percent differences that range from 11% to 30% (mean = 22%) from the depths of *WZ*98 measured for the same basins. These differences are also systematically smaller than *WZ*98, which may be related to our use of the median statistic and inclusion of measurements across a wider range of azimuths. In addition, several workers have begun to use LOLA topography to examine the depths of lunar basins [*Sori and Zuber.* 2011], but systematic geometric measurements of basins exhibiting peak-ring morphologies have yet to be conducted.

[31] Given the large azimuthal variation in basin topographies, our new depth data show general agreement with the *WZ*98 trend but with systematically smaller depths, ranging from 3.01 km to 6.40 km (Figure 9a). Schwarzschild, the smallest peak-ring basin, plots well below the *WZ*98 line, diverging more from the *WZ98* trend than all other peak-ring basins. Interestingly, the protobasin, Compton, also plots well below the *WZ*98 line and appears to form the tail end of a power law trend with peak-ring basins (Figure 9a). If this trend is real, it is steeper than the trend determined by *WZ*98, predicting shallower depths of 1–2 km at the smallest basin sizes (Figure 9a). The depths of peak-ring basins are also smaller than extrapolation of the trend of depths for complex craters >15 km determined by *Pike* [1974] (Figure 9a). The depths of Antoniadi and Hausen are more comparable to the *Pike* [1974] trend for complex craters, suggesting an incomplete transition to peak-ring basins. The ratio of depth to diameter is also observed to decrease with increasing rim-crest diameter for peak-ring basins (Figure 10a).

[32] While our measurements of the basin depth are statistically more representative than previous depth measurements, it is unclear whether the steeper depth-diameter trend revealed for peak-ring basins and the protobasin, Compton, (Figure 9a) is a real product of the impact process and transition to peak-ring basins or the result of variations in crater degradation process or impact conditions. The formation of this trend relies on only two basins, Schwarzschild and Compton, and it is not a statistically confident interpretation of the entire data set. In order to make a more informed interpretation of the trend revealed by our new depth data, we now discuss several factors that may be contributing to the small depth-diameter ratios at the smallest basin diameters, and in particular Schwarzschild and Compton.

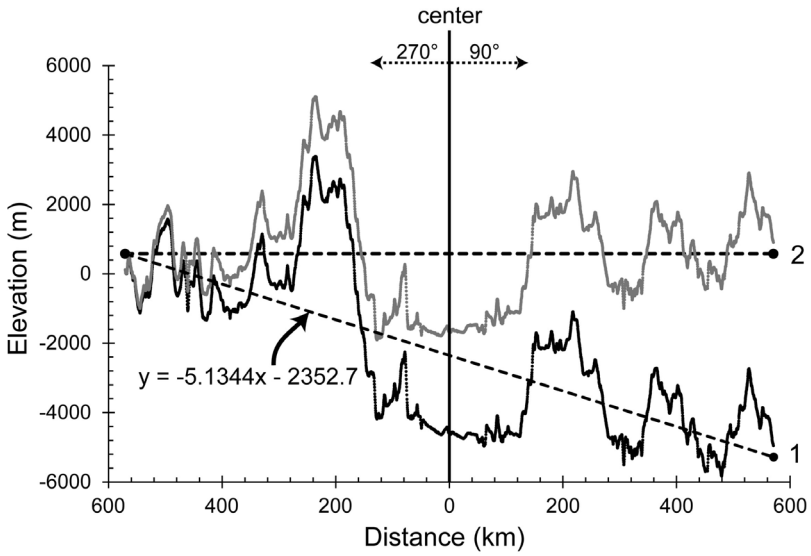

Figure 8. Example of how profiles were corrected for regional slope (section 4.5). In this case for Schrödinger basin, two complementary radial profiles (90° and 270° azimuth) produce a regional slope that dips toward the east (Figure 3b). This slope is removed by fitting a line to the profile (line 1 and equation) and leveling it out to a line of zero slope (line 2). This procedure was completed for each complimentary pair of profiles to determine the effect of regional slope on our topographic calculations. We found <10% difference between parameters corrected and not corrected for regional slope and, therefore, chose to only report uncorrected values in this study (see section 4.5).

[33] First, the reduced depths may be a result of volcanic infilling, tectonic processes or ejecta emplacement. We rule out shallowing by volcanism in Schwarzschild, because previous mapping [*Lucchitta*, 1978] and our own morphological observations indicate a lack of features that would be indicative of mare volcanic resurfacing within its interior. Due to the presence of mare-like material within Compton [*Lucchitta*, 1978], it is possible that its reduced depth is related to infilling by volcanic material. However, the preservation of Compton's peak ring and central peak suggest that volcanic infilling was limited in thickness, perhaps shallowing its depth by only a few hundred of meters. Uplift of the floor from the processes forming its extensive network of floor fractures may have contributed to the depth shallowing. As mentioned, we observe no doming of topography within Compton, suggesting that the floor either relaxed or did not experience the substantial uplift experienced by other floor-fractured craters [*Schultz*, 1976].

[34] Like all basins on the Moon, the interiors of Schwarzschild and Compton have certainly been modified by the addition of impact ejecta into their interiors. The addition of ejecta from superposed craters and nearby basins throughout the lifetime of these basins (ages for these basins are generally Nectarian [*Wilhelms et al.*, 1987]) could have contributed to some shallowing of the interior of Schwarzschild. Schwarzschild also has a superposed impact crater near its center buffer zone, and although the crater was excluded from the center elevation calculations, the crater has certainly added ejecta material to the central portions of the basin. In order to account for the observed depths, however, ejecta infilling would have to reduce the depth of Schwarzschild by 1–2 km. While possible, the preservation

Table 5. Ratios of the Median Values of the Parameters Given in Table 4 for Peak-Ring Basins and Protobasins

		Ratios						
Name	D_r	d/D_r	h_{pr}/d	h_{cp}/d	h_{wall}/d	h_{floor}/d	W/r_r	r_{wb}/r_r
Peak-Ring Basins								
Schwarzschild	207	0.0145	0.2076	-	0.9349	0.0651	0.2475	0.7448
D'Alembert	232	0.0199	0.0911	-	0.8585	0.1415	0.2372	0.7579
Bailly	299	0.0138	0.2738	-	0.8360	0.1640	0.1972	0.7874
Schrödinger	326	0.0122	0.3370	-	0.9127	0.0873	0.2119	0.7795
Mendeleev	331	0.0167	0.1449	-	0.9526	0.0474	0.2567	0.7433
Korolev	417	0.0113	0.3010	-	0.8596	0.1404	0.1970	0.7911
Moscoviense	421	0.0152	0.5820	-	0.7504	0.2496	0.2334	0.7688
Apollo	492	0.0097	0.6139	-	0.7316	0.2684	0.1652	0.8130
Protobasins								
Antoniadi	137	0.0299	0.1566	0.1878	0.8489	0.1511	0.2712	0.7322
Compton	166	0.0145	0.1019	0.9661	0.9594	0.0406	0.2725	0.7233
Hausen	170	0.0349	0.0465	0.4195	0.9099	0.0901	0.3591	0.6298

of peak-ring topography within this basin precludes infilling by such a large volume of material.

[35] Second, reduction of the rim elevations by proximal weathering and superposed impact craters could contribute to the shallow observed depths [*Head*, 1975]. This could be the case for Class III and IV degraded basins (Table 1), where superposed and adjacent craters have reduced the topography of portions of the basin rims. Schwarzschild and Compton are Class II and I basins (Table 1), and have relatively fewer superposed impacts; these superposed craters

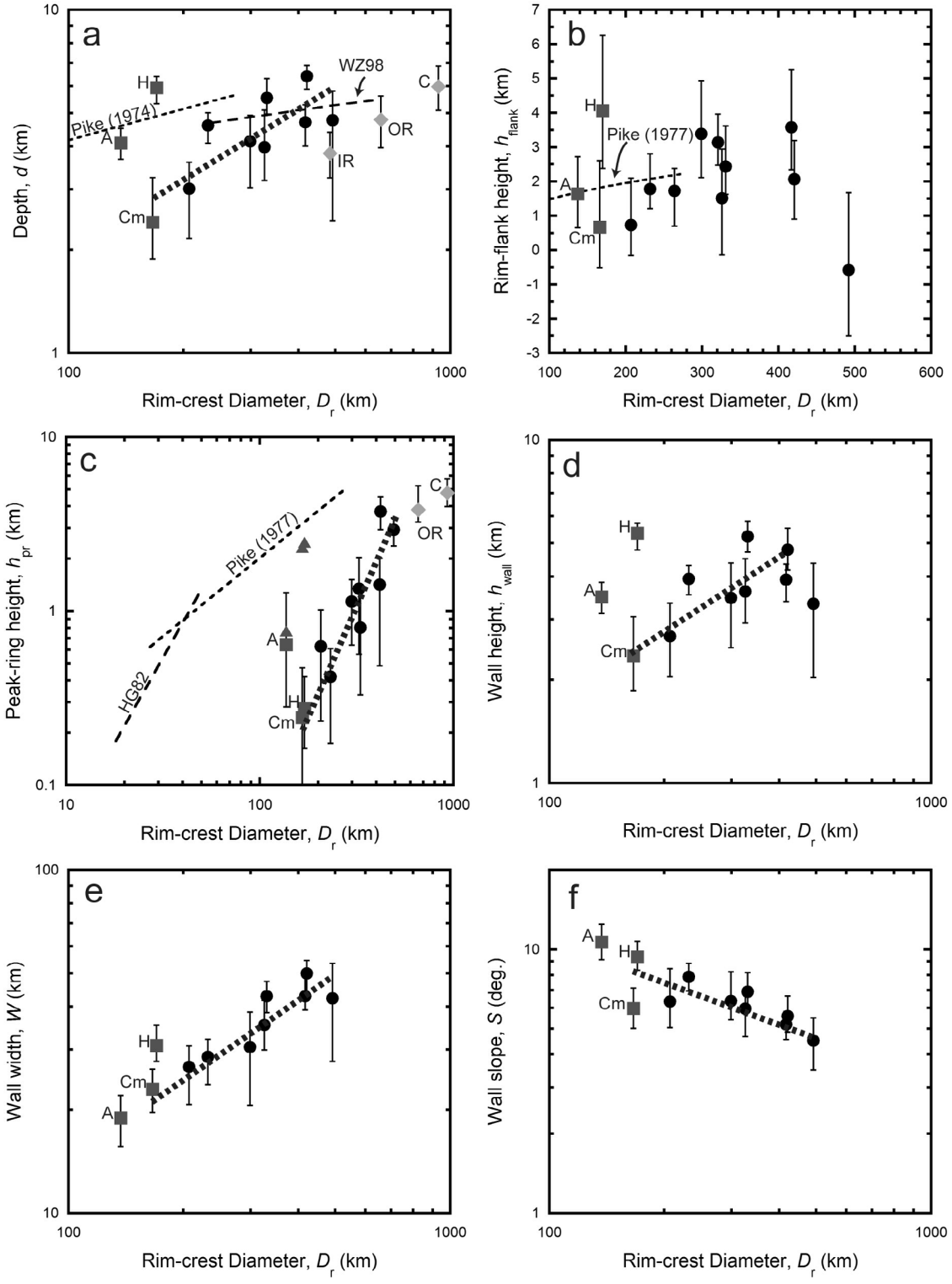

Figure 9

were also excluded from our statistical analysis (see section 4), leaving only the morphologically "freshest" portions of the rim for geometric calculations. Furthermore, the third quartile statistics of the depths for Schwarzschild and Compton are still >1 km shallower than the *WZ*98 line (Figure 9a). Therefore, while reduction in rim elevation may be affecting the statistics, it is not enough to account for the substantially smaller depths that we measure.

[36] Third, the shallowing could be the result of differences in impact conditions and target properties. *Sori and Zuber* [2011] suggest that some basins could be shallower in the vicinity of South Pole-Aitken basin due to greater geothermal flux and increased viscous relaxation. Viscous relaxation of lunar impact basins has been suggested to be an effective shallowing mechanism for some older impact basins, with geographical differences in heat flux affecting the degree of this shallowing in these impact basins [*Solomon et al.*, 1982]. From our observations, we do not see any clear correlation between geography and the depth/diameter ratio of peak-ring basins or protobasins. Differences in the angle of impact and ruggedness of pre-existing topography could also affect the final basin depth. More oblique impacts can act to reduce the cratering efficiency (i.e., the ratio of the mass of excavated material to the mass of the impactor) of the impact event, which could account for the shallow depth of Compton compared to Antoniadi, Hausen, and complex craters of similar diameter [*Pike*, 1974]. However, no substantial offset or anomalies in the morphologies of central peak structures is observed in Compton or Schwarzschild (Table 6), which might be indicative of an oblique impact [*Schultz*, 1992a; *Schultz and Stickle*, 2011]. The fact that Compton impacted into the rim of the multi-ring basin, Humboldtianum, may have influenced its final topography; however, it is unclear if this would contribute to shallowing of the basin's depth.

[37] Finally, the depth-diameter trend in Figure 9a may be a direct result of the transition from complex craters to peak-ring basins. The depths and diameters of the protobasins, Antoniadi and Hausen, are comparable to those of complex craters on the Moon [*Pike*, 1974] (Figure 9a). Compton, however, plots at the tail-end of the apparent trend for peak-ring basins, with a depth/diameter ratio of 0.015. If Compton's shallow depth is not completely a product of post-impact modification, it may be reflecting a real result of the transition to peak-ring basins. This would be consistent with the comparably shallow depth of the smallest peak-ring basin, Schwarzschild, and could reflect a combination of non-proportional scaling of the excavation cavity geometry at large crater sizes, increased floor uplift, and an increase in listric faulting of the basin walls (see section 6). Unfortunately the lack of well-preserved protobasins and peak-ring basins within the transitional diameter range on the Moon does not permit an unambiguous interpretation of these observations.

[38] In summary, our plot of the depth-diameter relationship for protobasins and peak-ring basins reveals a possible steeper trend than previous measurements from *Williams and Zuber* [1998]. However, due to the limited number of preserved peak-ring basins and protobasins on the Moon, an unambiguous interpretation of this trend, especially at the smallest basin diameters, is difficult. What is more clear is the overall reduction in the depth/diameter ratio for peak-ring basins, compared with complex craters. This reduction in the depth/diameter ratio was observed by *Williams and Zuber* [1998] and is supported by our new data. Similar depth-diameter calculations for planetary bodies with a greater population of peak-ring basins and protobasins (e.g., Mercury; *Baker et al.*, 2011b) may help to resolve this ambiguity in the lunar depth-diameter trend.

5.2. Rim-Flank Height (h_{flank})

[39] The height of the rim flank is important for use in examining the amount of rim uplift, decay of ejecta with distance from the crater rim and for estimating the thickness of plains and mare material from buried impact craters [*Pike*, 1977; *Head*, 1982]. *Pike* [1977] defined relationships between rim-flank height (or his "rim height") and diameter for craters <15 km ($h_{\mathrm{flank}} = 0.036D_{\mathrm{r}}^{1.014}$) and >15 km ($h_{\mathrm{flank}} = 0.236D_{\mathrm{r}}^{0.399}$) on the Moon. He noted that the change in slope between the two trends indicated a transition from simple to complex craters, likely to be the result of the onset

Figure 9. Log-log plots of derived parameters (Table 4) for protobasins (dark gray squares, A = Antoniadi, Cm = Compton, H = Hausen), peak-ring basins (black circles), and the rings of Orientale basin (light gray diamonds, IR = Inner Rook, OR = Outer Rook, C = Cordillera). All parameters are plotted as a function of the rim-crest diameter, as reported by *Baker et al.* [2011a] (Table 1). Data points are median values and the errors bars are the interquartile range of the data set. The heavy dashed lines denote qualitative trends interpreted from the data. (a) Basin depth (*d*). The depth trend determined for lunar complex craters [*Pike*, 1974] is shown for reference. Also shown is the depth trend determined for lunar basins from *Williams and Zuber* [1998] (WZ98). Peak-ring basins and the protobasin, Compton, may form a steeper power law trend than determined by *Williams and Zuber* [1998]. The depths for the Inner Rook and Outer Rook rings of Orientale are shallower than extrapolation of the trend of *Williams and Zuber* [1998] and our new peak-ring basin measurements. The Cordillera ring is more in-line with the observed peak-ring basin trends. (b) Rim-flank height plotted with linear axes. The trend of rim-flank height determined for lunar complex craters is also given [*Pike*, 1977]. Points are very scattered, resulting from the difficulties in determining this parameter accurately. Negative values result from the target reference point being at a higher elevation than the rim-crest reference point. (c) Peak-ring height. Plotted are the trends for central peak heights in complex craters determined by *Hale and Grieve* [1982] (HG82) for small diameters and by *Pike* [1977] for larger complex craters. Peak-ring heights for peak-ring basins form a trend similar to central peak heights in small complex craters (HG82), although shifted toward larger rim-crest diameters. The plots for Orientale give the height of the equivalent of a "peak ring" for the Outer Rook ring (peak ring = Inner Rook ring) or the Cordillera ring (peak ring = Outer Rook ring). (d) Wall height generally increases with increasing rim-crest diameter, although the data are more scattered and could be consistent with a flatter trend. (e) Wall width increases in a well-defined manner with increasing rim-crest diameter. (f) Wall slope decreases with increasing rim-crest diameter, due to the increase in wall width without a proportional increase in wall height.

of terracing of the rim wall within complex craters and the formation of central peaks.

[40] We plot the rim-flank heights for protobasins and peak-ring basins versus rim-crest diameter in Figure 9b. While there is much scatter, the rim-flank height appears to roughly follow an extension of the rim height trend for craters >15 km determined by *Pike* [1977]. The extreme scatter in our data is due to the very irregular topography that accompanies estimation of the target elevation. Impact craters within the target buffer (Figure 3a) can dramatically increase or decrease the calculated rim-flank height depending on whether the profile lies within the crater

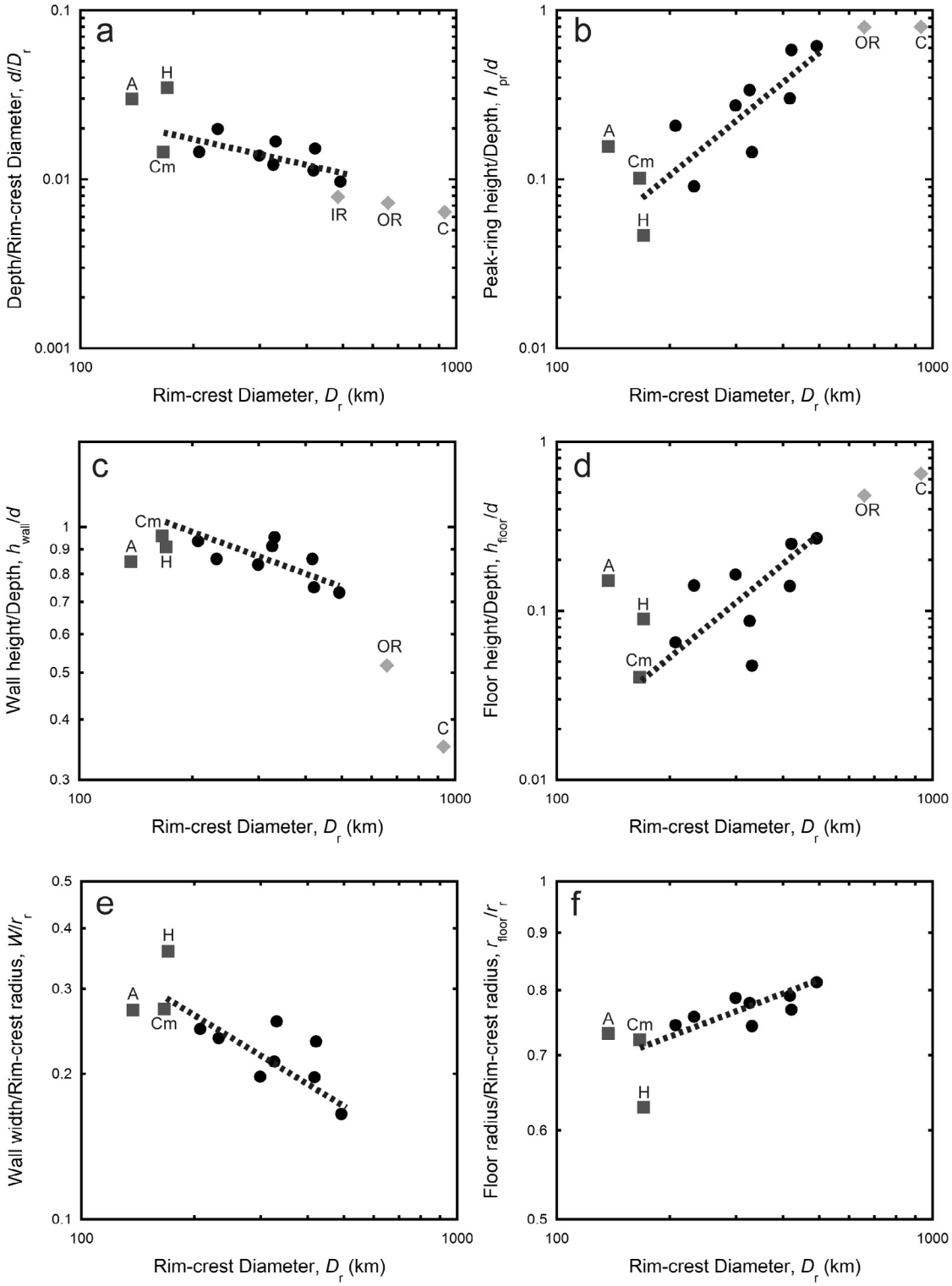

Figure 10

Table 6. Data for Determining the Peak-Ring Offset Direction and Magnitude[a]

Name	D_r	Lat_D_r	Lon_D_r	$D_{pr,fit}$[b]	Lat_$D_{pr,fit}$[b]	Lon_$D_{pr,fit}$[b]	Offset Distance (km)	Offset Azimuth (°)	Ring Elevation at Offset (km)[c]	Percentile[d]	Rim Elevation at Offset (km)[c]	Percentile[d]
Schwarzschild	207	70.3554	120.0916	61	70.0335	120.2059	9.83	173	-	-	0.84	0.90
D'Alembert	232	51.0543	164.8361	105	51.1668	164.6340	5.14	312	-	-	3.04	0.44
Bailly	299	−67.1813	−68.7959	134	−67.0459	−68.4476	5.81	45	−0.46	0.47	1.48	0.16
Schrodinger	326	−74.9047	133.5332	155	−74.7908	133.8736	4.38	38	−4.08	0.22	−1.79	0.11
Mendeleev	331	5.4436	141.1357	141	5.5547	141.5526	13.03	75	-	-	2.97	0.07
Korolev	417	−4.4430	−157.4701	201	−4.2140	−158.0561	19.03	291	4.25	0.60	7.03	0.33
Moscoviense	421	26.3355	147.3612	192	25.4982	146.4695	35.16	224	1.49	0.92	2.77	0.29
Apollo	492	−36.0934	−151.4845	252	−36.0985	−150.6966	19.31	91	-	-	0.10	0.72

[a]The diameters and center coordinates for circle fits to the rim crest [from *Baker et al.*, 2011a] (same as Table 1) and peak ring are shown for each basin. Also given are the offset distances and offset direction (i.e., azimuth), as well as the average elevations and the percentiles of the peak-ring and rim-crest elevations in the offset direction.

[b]Peak-ring diameter ($D_{pr,fit}$) in kilometers and center latitude (Lat_ $D_{pr,fit}$) and longitude (Lon_ $D_{pr,fit}$) of a small circle fit to the peak ring reference points for each basin.

[c]Ring and rim elevations were taken as an average over 10° of azimuth centered on the offset azimuth.

[d]The elevations of the peak ring and rim crest calculated as percentiles of the entire set of elevations for each basin.

interior or on its rim. While use of the median value and interquartile range should limit the influence of extrema in the calculated values, the highly irregular topography of the lunar highlands makes accurate determination of the target elevation difficult [*Pike*, 1976]. Apollo's rim-flank height is a negative value because the target surface is at an elevation that is generally greater than the rim-crest elevation (Table 3). This is largely due to Apollo's impact into the rim wall of South Pole-Aitken basin [*Garrick-Bethell and Zuber*, 2009]. Correcting for the regional slope caused by South Pole Aitken basin (section 4.5, Figure 8) still results in a negative value for the rim-flank height. This example suggests that pre-existing topography can highly influence determination of the rim-flank height even when corrected for regional slope. Calculating the rim-flank height for basins on the Moon is thus inherently difficult, and an improved technique for measuring this parameter is needed if its value is to be calculated accurately. Due to the highly variable nature of our rim-flank height measurements, we do not attempt to identify unique trends in the data but rather suggest that rim-flank height for protobasins and peak-ring basins may be roughly estimated by an extension of the *Pike* [1977] trend to peak-ring basin diameters.

5.3. Wall Width (W), Height (h_{wall}) and Slope (S)

[41] Other important geometric parameters deal with the crater wall. Measurements for the wall height and width were not explicitly included in the lunar crater catalog of *Pike* [1976]; however, wall slope was calculated, plotted as the tangent of the slope of the rim wall [*Pike*, 1977]. Since wall slope (S) is directly calculated from the values for wall width (W) and wall height (h_{wall}), we begin with a discussion of the trends for these two parameters as a function of rim-crest diameter.

5.3.1. Wall Width (W)

[42] Wall width is observed to increase in a well-defined manner as a function of rim-crest diameter for peak-ring basins and protobasins (Figure 9e). This increase in wall width is expected due to the increase in gravitational instability of the rim, which results from increased energy of impact, a deeper excavation cavity, and subsequent increase in gravitational potential and slumping of the rim wall. Interestingly, the ratio of the wall width to the crater radius (W/r_r), indicates a general decreasing trend with increasing rim-crest diameter (Figure 10e). A consequence of this trend is an associated increase in the fraction of floor material with increasing rim-crest diameter (i.e., increasing r_{floor}/r_r ratios) (Figure 10f). These observations are in line with previous observations that noted that flat floors in fresh craters >20 km in diameter comprise increasingly larger fractions of the crater interior, or rim-crest diameter, with increasing crater size [*Pike*, 1977]. Wall widths decrease from ∼30% to ∼17% of the rim-crest radius from protobasins to the largest peak-ring basins (Figure 10e), with an accompanying increase in the radius of the floor from ∼70% to ∼83% of the rim-crest radius (Figure 10f). In summary,

Figure 10. Log-log plots of the ratios of derived parameters for protobasins (dark gray squares, A = Antoniadi, Cm = Compton, H = Hausen), peak-ring basins (black circles), and the rings of Orientale basin (light gray diamonds, IR = Inner Rook, OR = Outer Rook, C = Cordillera) (Table 5). All parameters are plotted as a function of the rim-crest diameter, as reported by *Baker et al.* [2011a]. Data points are median values. Error bars are not plotted for clarity, as these can be very large due to the highly variable nature of the calculated parameters (Figures 6 and 7). The heavy dashed lines show qualitative trends interpreted from the data. (a) Basin depth (d) to rim-crest diameter (D_r) ratio slightly decreases with increasing rim-crest diameter. The ratios for the rings of Orientale plot below an extrapolation of the peak-ring basin trend. (b) Peak-ring height to depth ratio increases for peak-ring basins. This trend is not maintained for Orientale basin. (c) Wall height to depth ratio decreases for peak-ring basins; however, the scatter in the data and subtly of the trend could also be consistent with a flatter trend. The rings of Orientale have very small ratios compared to peak-ring basins. (d) Floor height to depth ratio increases with increasing rim-crest diameter, with the trend extending to Orientale basin. (e) Wall-width to rim-crest radius ratio decreases due to possible masking of the toes of rim-wall slump blocks by impact melt. (f) Floor radius to rim-crest radius ratio increases with increasing rim-crest diameter, consistent with the trends observed within complex craters [*Pike*, 1977].

while the wall width is increasing with increasing rim-crest diameter (Figure 9e), due to an increase in the amount of rim-wall slumping, the wall width is actually decreasing relative to the rim-crest diameter (Figure 10e) and the crater floor is comprising a larger areal fraction of the crater interior (Figure 10f).

5.3.2. Wall Height (h_{wall})

[43] At the same time that the wall width is increasing with rim-crest diameter (Figure 9e), the wall height is increasing at a much smaller rate (Figure 9d). Furthermore, a plot of the ratio of wall height to depth (h_{wall}/d) (Figure 10c) suggests that this ratio may be slightly decreasing with increasing basin size. We note that the data in Figures 9d and 10c are more scattered than for other measured parameters, opening up the possibility of other interpretations (e.g., flat versus increasing or decreasing trends). Despite this ambiguity, we interpret the data to reflect real variations in the wall height as a function of the basin diameter, which appear more in line with corresponding trends in other measured parameters, such as wall width (Figures 9 and 10).

[44] Our interpretations of the wall height data have several implications. First, they indicate that most of the trend in wall slope with increasing rim-crest diameter (Figure 9f) is caused by the much more prominent trend of increasing wall width (Figure 9e and section 5.3.3) than wall height. Second, a decrease in the h_{wall}/d ratio indicates that the fraction of the total depth contributed by the floor height is increasing with increasing rim-crest diameter (i.e., the h_{floor}/d ratio is increasing) (Figure 10d). This trend is consistent with the observation of a small central depression in the center of some of the largest peak-ring basins (notably Korolev, Moscoviense and Apollo). Lowering of the center elevation within these basins by development of a central depression may be one deepening mechanism for peak-ring basins at the largest rim-crest diameters. It is possible that the increase in floor height and formation of central depressions may be a result of expulsion of impact melt from the basins' central melt cavities, which is then deposited on the floor exterior to the peak ring and on the rim walls and basin exterior. Redistribution of impact melt within the basin may also offer an explanation for the decreasing h_{wall}/d and W/r_r ratios (Figures 10c and 10e). Burial of the toes of slump blocks by increased volumes of expelled impact melt would act to mask the identification of these features in topographic analyses, thereby decreasing the apparent height and width of the basin wall and increasing the apparent floor diameter (see section 6 for a more detailed discussion).

5.3.3. Wall Slope (S)

[45] *Pike* [1977] noted that the wall slope increases gradually from 19° to 29° for craters between 0.5 km to 20 km and then sharply decreases to 14° at 50–60 km diameter and to about 7° for the largest crater (~300 km). Our new slope measurements confirm this general decreasing trend in wall slope for peak-ring basins and protobasins (Figure 9f). There is a general decrease in wall slope from about 9–10° for protobasins to about 4–5° for the largest peak-ring basins. As mentioned in section 5.3.2., most of this decrease in wall slope is due to an increase in wall width, without a proportional change in the wall height. These wall slopes are much lower than those observed for complex craters and the protobasins Antoniadi and Hausen, which have median slope values of about 10° (Figure 10), [*Pike*, 1977]. As with wall width, this decreasing trend in the wall slope is likely to be due to the increase in the amount of wall slumping, resulting from the increase in gravitational instability of the rim that accompanies high-energy impacts.

5.4. Peak-Ring Height (h_{pr})

[46] The height of the peak ring for basins is a poorly defined parameter that has only a limited number of measurements. The height of central peaks (h_{cp}) as a function of the rim-crest diameter has a more well-defined relationship [*Pike*, 1977; *Hale and Grieve*, 1982]. *Pike* [1977] defined a positive power law relationship of $h_{cp} = 0.032D_r^{0.900}$ between central peak height and rim-crest diameter for craters >27 km in diameter. *Hale and Grieve* [1982] determined a steeper trend for central peak heights in the smallest complex craters from 17 to 51 km in diameter ($h_{cp} = 0.0006D_r^{1.97}$). *Hale and Grieve* [1982] also noted a decreasing slope in the $h_{cp}-D_r$ trend at the largest complex crater diameters, which fell on a trend similar to that of *Pike* [1977].

[47] The peak-ring heights (h_{pr}) for peak-ring basins and protobasins are plotted as a function of rim-crest diameters (D_r) in Figure 9c. As shown, there is a well-defined increase in the peak-ring height from about 0.2 km to 4 km as a function of rim-crest diameter, with markedly smaller peak-ring heights than what is predicted by extrapolation of the central peak height trend of *Pike* [1977] for craters >27 km. The $h_{pr}-D_r$ trend, however, has a very similar slope to the $h_{cp}-D_r$ trend of *Hale and Grieve* [1982] but shifted toward larger diameters. These similarities suggest that the energy of impact may also be controlling the height of peak rings in peak-ring basins [*Hale and Grieve*, 1982]. Interestingly, the protobasins with the smallest peak-ring heights (Compton and Hausen), also have the largest central peak heights that plot near the *Pike* [1977] trend (Figure 9c, triangles). Antoniadi has a large peak-ring height at 0.65 km relative to Compton and Hausen (~0.25 km), with a correspondingly smaller central peak height at 0.77 km compared to Compton and Hausen (~ 2.4 km). These observations are consistent with observations of *Hale and Grieve* [1982], who noted that a reduction in the central peak height for large complex craters is accompanied by a ring of roughening that could represent a redistribution of uplifted material at the transition from complex craters to peak-ring basins. Under this model, the trend for protobasins should involve decreasing central peak heights and increasing peak-ring heights with increasing rim-crest diameter. While the relationship between central peak and peak-ring height holds for the three lunar protobasins (Figure 9c), the relationship with rim-crest diameter is reversed from what is expected from the model. Due to the small sample size, it is difficult to say with confidence whether this observation is a direct contradiction of the model or simply a product of differences in impact conditions, such as velocity and angle of impact. Observations from the much larger protobasin and peak-ring basin populations on Mercury [*Baker et al.*, 2011b] may be able to provide a more comprehensive test of this model.

[48] The ratio of the peak-ring height to basin depth (h_{pr}/d) is also plotted as a function of rim-crest diameter in Figure 10b, indicating that the h_{pr}/d ratio also increases as a function of rim-crest diameter. The cause of this increase in the h_{pr}/d ratio could be twofold. A similar increase in the

ratio of h_{cp}/d is predicted from the height and depth relationships from *Pike* [1977] and *Hale and Grieve* [1982]. For complex craters, this suggests that the magnitude of floor uplift is increasing at a greater rate than the magnitude of crater deepening with increase in crater diameter. Therefore, the process controlling floor uplift and central peak formation becomes more important with increasing size of the impact event. This argues for an energy dependent variation in central peak height. A similar interpretation of the trend in h_{pr}/d may be made, with the process controlling uplift and peak-ring formation becoming increasingly more important with increasing size of the basin-forming event. In addition to peak-ring uplift, an important contribution to the increasing h_{pr}/d ratio trend is increasing basin floor relief (Figure 10d). As discussed in section 5.3.2, while the depth/diameter ratio of peak-ring basins decreases with increasing diameter, the floor height (i.e., relief from the base of the crater wall to the center) comprises a larger fraction of the total depth of the basin. Similarly, this relative increase in floor height is likely to be at least partially contributing to the increase in h_{pr}/d for peak-ring basins, due to the nature in which peak-ring height is calculated (Table 2).

5.5. Wall Slumping and Peak-Ring Formation

[49] Early questions about the origin of central peaks within complex craters involved the contribution of rim-wall slumping to the formation and resulting height of the central peak [*Pike*, *1977*; *Melosh*, 1989]. To address this question for the peak rings in peak-ring basins, we attempted to identify correlations between the peak-ring elevation and various geometric parameters of the rim and basin wall. If rim-wall slumping had an effect on peak-ring formation, one might expect some correlation between the distance to the base of the wall with peak-ring elevation (e.g., enhanced listric faulting produces more prominent peaks). To evaluate if such a correlation exists, we plot the correlation coefficient (R) and coefficient of determination (R^2) of linear fits to peak-ring elevations and various ratios for each set of basin profiles. We use the ratio of the peak-ring radius to the radius of the wall base (r_{pr}/ r_{wb}) as a proxy for proximity to wall slump material. We also examined correlations with the ratio of the peak-ring radius to the rim-crest radius (r_{pr}/ r_r). As shown in Figures 11a and 11b, the correlation coefficients show no systematic linear correlations between the relief of the peak ring and distance to the base of the wall or the distance to the rim crest. In fact, a strong anti-correlation (negative correlation coefficients) is found for Korolev, while a strong positive correlation is found for Moscoviense. To first-order, these observations suggest that proximity to the rim wall does not heavily influence the final topography of the peak ring.

[50] It is interesting, however, that there appears to be some general positive correlation (with Bailly as the clear exception) between the height of the peak ring and height of the rim crest (Figure 11c). This suggests that variations in pre-existing topography may exhibit some control on the topographic characteristics of peak rings. This is most clearly seen in the cases where impact basins are formed on or near the rim of even larger basins such as South Pole-Aitken (SPA). Both Schrödinger and Apollo have impacted into the rim or rim wall of SPA [*Garrick-Bethell and Zuber*, 2009], and both have rim-crest elevations and peak-ring elevations that are enhanced toward the rim of SPA, with reductions in elevation occurring at azimuths directed downslope toward the center of SPA (e.g., Figure 3). This idea is consistent with observations of terrestrial impact structures such as Chicxulub, where topographic lows in the pre-impact terrain can result in more subdued topography of the rim and peak ring [*Gulick et al.*, 2008].

5.6. Peak-Ring Offset

[51] We also measured the direction and magnitude of offset of the peak ring relative to basin rim crest for peak-ring basins (Table 6). Peak-ring offset was measured by calculating the distance and azimuth between the centroids of circle fits to the rim crest and the peak ring. We used the centroid coordinates for the rim-crest diameter of *Baker et al.* [2011a] (Tables 1 and 6) and calculated the centroid of the peak ring by numerically fitting a small circle to the peak-ring reference points. Circle fits to the peak-ring reference points were obtained by using the FITCIRCLE program available from the Generic Mapping Tools (GMT) analysis package [*Wessel and Smith*, 1991]. This program minimizes the sum of squares of cosines of angular distances of a small circle fit to a series of points on a sphere.

[52] We find that peak rings are typically offset with respect to the rim-crest centroid by an average of 13 km and a range of 3 to 35 km (Table 6). It has been hypothesized that the magnitude and direction of offset in peak rings may reflect the impactor approach direction and angle of impact. Oblique impacts result in a reduction in cratering efficiency and asymmetries in the depths of excavation (i.e., deepening in the up-range direction), which may influence the topography and location of central uplift structures [*Schultz*, 1992a, 1992b]. *Schultz* [1992a, 1992b] and *Schultz and Stickle* [2011] suggest that oblique impacts can produce peak rings that are 1) offset in the up-range direction due to a deeper cavity and greater compression/elastic rebound in this direction, 2) elongate along the trajectory axis, and 3) breached in the downrange direction due to scouring by impactor decapitation. While the direction of impactor approach may be inferred from analyzing the distribution and patterns of ejecta and secondaries [*Schultz*, 1992a; *Ekholm and Melosh*, 2001; *McDonald et al.*, 2008], the highly modified nature of the ejecta of peak-ring basins analyzed in this study makes it difficult for these estimates to be made. Ejecta patterns are much more distinct on Venus and have been used to infer the direction of approach for some peak-ring basins [*Schultz*, 1992a; *Ekholm and Melosh*, 2001; *McDonald et al.*, 2008]. However, comparisons between these inferred approach directions and directions of peak-ring offset found little correlation between the two parameters [*McDonald et al.*, 2008]. This suggested that impactor approach may have little, if any, influence on the offset direction of peak rings and that perhaps target heterogeneities are more important. It is also possible that the initial offset in peak-ring position may be masked by increased rim-wall slumping and widening of the rim wall in the up-range direction [*Schultz*, 1992b; *Ekholm and Melosh*, 2001].

[53] One prediction of the hypothesis of *Schultz* [1992a, 1992b] is that the topography of the peak ring should be enhanced in the up-range direction and, therefore, in the direction of offset in the peak ring. Additionally, greater

deepening of the cavity in the up-range direction also predicts there to be an enhancement in rim-crest elevation in the up-range or offset direction. We evaluate these predictions by examining if any correlation exists between the peak-ring offset and elevation of the peak ring and rim crest in this direction (Figure 12). We evaluated the elevation of the peak ring and rim crest in direction of offset as percentiles of the entire set of peak-ring and rim-crest elevation measurements. Unfortunately, the peak-ring elevation for only four basins could be evaluated due to the overlap in offset direction with peak-ring exclusion zones. We see that while enhancement of the peak ring in the direction of offset is clear for Moscoviense (the peak-ring elevation is at the 92nd percentile in the offset direction), this is not obvious for the other three basins (peak-ring elevation percentiles are between 22 and 60 in the offset direction). It is possible that smaller 5–10 km offsets may reflect more vertical impacts, and differences in the asymmetry of excavation may not be sufficient at these impact angles to record signification trajectory-dependent variation in peak-ring topography. This is consistent with an apparent dependence on peak-ring enhancement with magnitude of the peak-ring offset (Figure 12). Furthermore, we see no correlation between magnitude of the peak-ring offset and rim-crest elevation. In particular, Moscoviense, which has the largest peak-ring offset and is the best candidate for being produced by an oblique impact [*Schultz and Stickle*, 2011], has a rim-crest elevation at about the 30th percentile in the offset direction. This observation is in contrast to the predicted deepening of the crater in the up-range direction [*Schultz*, 1992a, 1992b]. As suggested by *McDonald et al.* [2008] for peak-ring basins on Venus, target properties may have a more dominant control on the offset in peak rings. For Moscoviense, offset in the peak ring could have been influenced by impact into an older basin with already thinned crust, as supported by geophysical observations [*Ishihara et al.*, 2011].

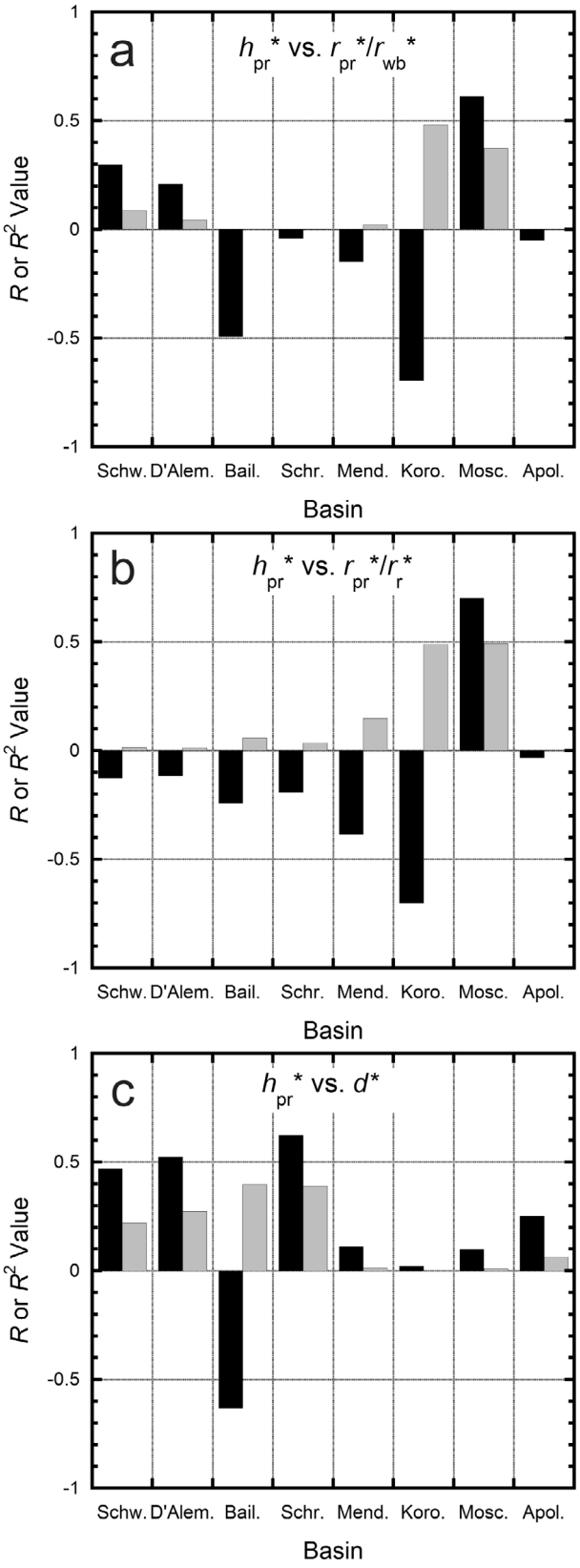

Figure 11. Correlation coefficient (R, black bars) and coefficient of determination (R^2, light gray bars) determined for each basin from linear fits to all azimuthal calculations of the height of the peak ring versus the (a) ratio of the peak-ring radius to the wall-base radius, (b) ratio of the peak-ring radius to the rim-crest radius, and (c) basin depth. The ratio of the peak-ring radius to the wall-base radius is used as a proxy for proximity to rim-wall slump material. No general correlation is found between peak-ring heights and this ratio (Figure 11a). No correlation is found between peak-ring heights and proximity to the rim crest (Figure 11b). Slightly greater correlation is found between peak-ring height and rim-crest height (Figure 11c), which may suggest that pre-impact topography is important in determining peak-ring topography.

5.7. Basin Volume (V_1 and V_2)

[54] As expected from the strong control that rim diameter has in determining the basin volume (equation (1)), the volumes of peak-ring basins and protobasins are observed to increase in a well-defined manner with increasing rim-crest diameter (Figure 13). The volumes calculated using both the double frustum method and the surface-to-TIN method (section 4.4) yield very similar results, with an average percent difference of about 3% (Table 4); there was also no systematic difference between the two methods. These results suggest that the double frustum method is a reliable method for calculating the volumes of peak-ring basins and

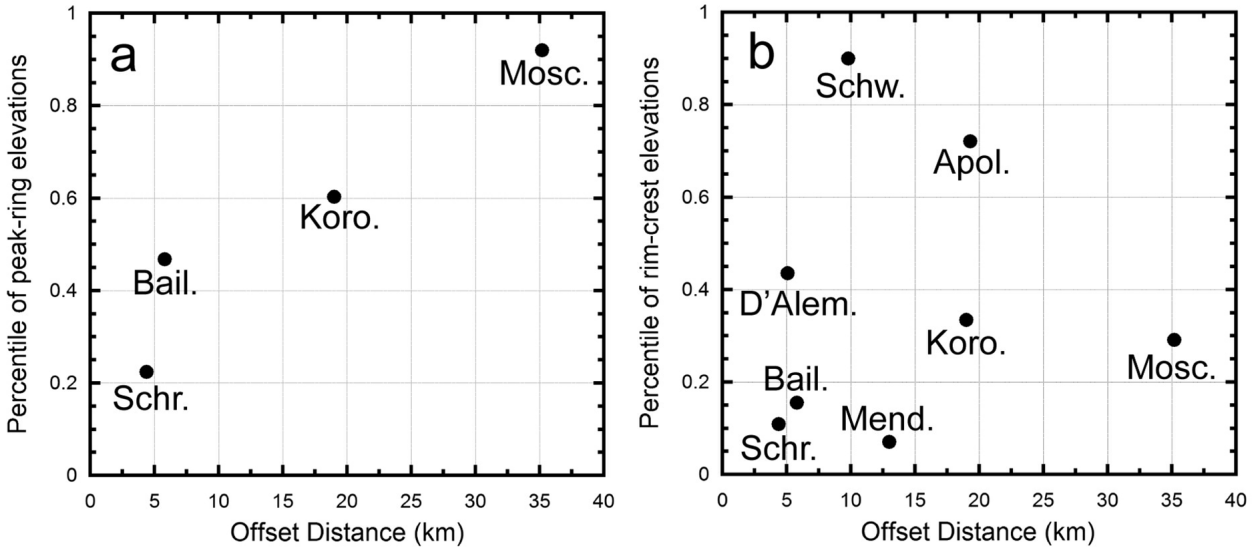

Figure 12. Plots of the percentile of the average elevation of the (a) peak ring and (b) rim crest in the direction of the peak-ring offset, as a function of the magnitude of the peak-ring offset (Table 6). Labels correspond to the first four letters of the names of peak-ring basins in Table 6.

protobasins. For perspective, the smallest peak-ring basin is comparable to the volume of the Caspian Sea on Earth (at 78,200 km^3), with the largest peak-ring basin being a factor of nine larger in volume.

[55] We also compared our calculated volumes for protobasins and peak-ring basins with the predicted volumes of a paraboloid fit to the depths and diameters of excavation cavities determined from gravity and topography observations of lunar impact basins [*Wieczorek and Phillips*, 1999] (Figure 13). The estimated volumes of these excavation cavities are based on an excavation depth-diameter relationship of $d_{ex} = (0.115 \pm 0.005)D_{ex}$ from *Wieczorek and Phillips* [1999]. To compare these excavation diameters with the final crater diameters of our measured data, we used the modification scaling relationship of *Croft* [1985] $(D_r \approx (D\mathrm{sc})^{-0.18}(D_{tc})^{1.18}$, where D_r is the final

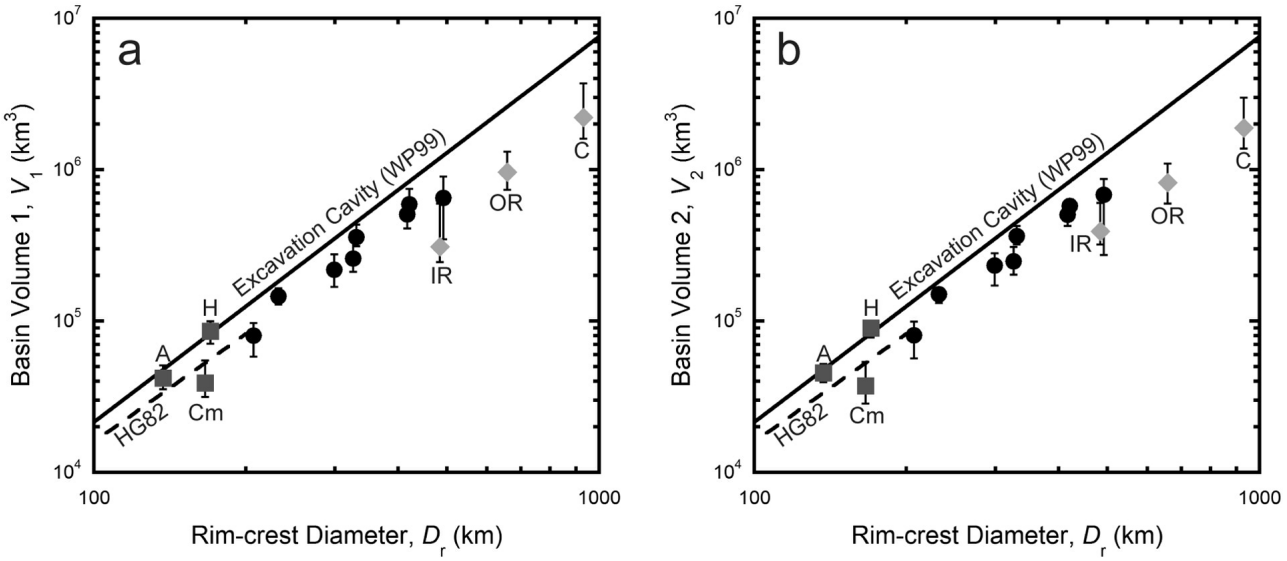

Figure 13. Volumes of protobasins (dark gray squares, A = Antoniadi, Cm = Compton, H = Hausen), peak-ring basins (black circles), and the rings of Orientale basin (light gray diamonds). The volumes are calculated using the (a) double frustum method (V_1, equation (1)) and (b) surface-to-TIN method (V_2) (see section 4.4 for a description of these methods). Also plotted in Figure 13a are the volumes of the excavation cavity for impact basins on the Moon, as predicted from geophysical measurements [*Wieczorek and Phillips*, 1999] (WP99). The trend for the volumes of complex craters on the Moon from *Hale and Grieve* [1982] (HG82) is also plotted in both Figures 13a and 13b.

crater diameter, D_{tc} is the transient crater diameter, and D_{SC} is the simple to complex crater transition diameter on the Moon (~19 km) [*Pike*, 1988]). While there is a distinction between excavation diameter and transient crater diameter [*Holsapple*, 1993], *Wieczorek and Phillips* [1999] treat these equivalently, and we therefore chose to use the *Croft* [1985] scaling for converting to final crater diameters here. We find that the measured volumes of peak-ring basins on the Moon are about 40% smaller than the predicted volumes of their excavation cavities (Figure 13). If the geophysical constraints and scaling relationships of the geometries of the excavation cavities of lunar basins provide good estimates, then our observations suggest that large volume reductions of the transient cavities of peak-ring basins must occur during the modification stages of the impact event, which has been noted by previous authors [*Williams and Zuber*, 1998; *Wieczorek and Phillips*, 1999]. All of this translation must occur via vertical floor uplift due to a combination of gravitational collapse of the transient cavity, elastic rebound of the cavity floor and perhaps some contribution from mantle flow processes [*Melosh and McKinnon*, 1978].

6. Model of the Progression of Basin Geometries With Increasing Diameter

[56] The new geometric trends discussed in section 5 permit us to construct a general model for how the geometric properties of craters change in the transition from complex craters to peak-ring basins and finally to multi-ring basins. We illustrate this model schematically in Figure 14 and discuss how these trends may be interpreted, below.

6.1. Largest Complex Craters

[57] At diameters near the onset of protobasins (~150 km in diameter), the largest complex craters have a relatively high d/D_r ratio of around 0.030 (Figure 9a). The width of the crater walls make up about 30% of the crater interior (Figure 10e), with the crater floor materials (including the central peak) making up the other 70% of the crater interior (Figure 10f). Central peaks for the largest complex craters can reach heights of about 0.5 to as much as 0.8 of the total basin depth [*Pike*, 1977]. These high ratios of the central peak height to crater depth (h_{cp}/d) suggest that substantial uplift of the central points of the basin floor is occurring at these crater diameters. This floor uplift does not appear to be affecting the entire basin interior, however, as high d/D_r ratios are still maintained. The floor relief is also very low at h_{floor}/d ratios as little as 0.05, which is probably related to the substantial uplift of central peak material.

6.2. Onset of Peak Rings: Protobasins

[58] The onset of peak rings begins at the diameters of protobasins, which exhibit both a central peak and peak ring. Although the population of protobasins is small, these basin types are crucial to interpreting the transition to peak-ring basins. Most of the geometric properties of protobasins are similar to those of complex craters, with similar wall widths and height and depth to diameter ratios (Figures 9 and 10). The protobasin, Compton, however, exhibits a substantially reduced d/D_r ratio (0.015), suggesting that reduction in the d/D_r ratio as observed for the smallest peak-ring basins may start at the diameters of protobasins. The central peak heights of protobasins are generally less than those within complex craters, and this is probably due to redistribution of uplifted or collapsed material to form peak rings (Figure 14b) [*Hale and Grieve*, 1982]. The compromise between relative volumes of central peak material and peak-ring material is also reflected in the small peak-ring heights of protobasins relative to peak-ring basins (Figure 9c).

6.3. Onset of Peak Rings: Peak-Ring Basins

[59] At the onset of peak-ring basins, the d/D_r ratio is reduced from that of complex craters by a factor of two, resulting in values of around 0.015 to 0.020 (Figure 10a). This reduction in the d/D_r ratio marks an important geometric transition in the formation of peak-ring basins, which has been noted by previous authors [*Williams and Zuber*, 1998]. We interpret this reduction in the d/D_r ratio to be largely due to a combination of several factors. The first involves changes that affect the geometry of the excavation cavity. Crater scaling (i.e., changes in the aspect ratio of the excavation cavity with impact event size) is thought to be proportional with impact event size, even up to the diameters of peak-ring basins [e.g., *Wieczorek and Phillips*, 1999]. However, there is some evidence supporting shallowing of the excavation cavity due to non-proportional scaling of cavity geometries, particularly at a diameter-dependent change in crater morphologies such as in the simple to complex crater transition [*Schultz*, 1988]. As in the transition from simple to complex craters, the transition from complex craters to peak-ring basins may result from a similar non-proportional change in crater scaling. Regardless of whether crater scaling is proportional or non-proportional, reduction in excavation cavity depth due to collapse and modification of the excavation cavity appear necessary to account for the measured depth-diameter relationships of impact craters [*Pike*, 1980; *Schultz*, 1988] (Figure 13). The decrease in d/D_r ratio observed in the transition from complex craters to peak-ring basins could, therefore, result from increased listric faulting and inward translation of the basin wall, accompanied by an increase in uplift of the floor over a broader area due to increased impact energy and broader zone of impact melting within the central portions of the basin. The increase in wall slumping is supported by the observed increase in wall width (Figure 9e), decrease in wall slope (Figure 9f), and reduction of the h_{wall}/d ratio (Figure 9c). However, due to the topographic barrier of a peak ring and physical limitations of the run-out distances of slumped material, rim-wall slumping is unlikely to affect the very central portions of the basin (Figure 14b). More wholesale decrease in the floor elevation from a non-proportional change in crater scaling and floor uplift during the modification stage of the impact event is probably most important in producing the observed depth-diameter trends.

[60] The W/r_r ratio and h_{wall}/d ratios are also reduced from complex craters (Figures 10e and 10c). We interpret these trends to largely reflect re-distribution of impact melt within the basin interior. Impact melt is highly mobile during the impact event due to the large-scale translations and momentum transfers that occur during excavation and modification of the transient cavity. Based on observations of ejecta patterns from craters on Earth and the terrestrial planets, ejection of impact melt from craters has been

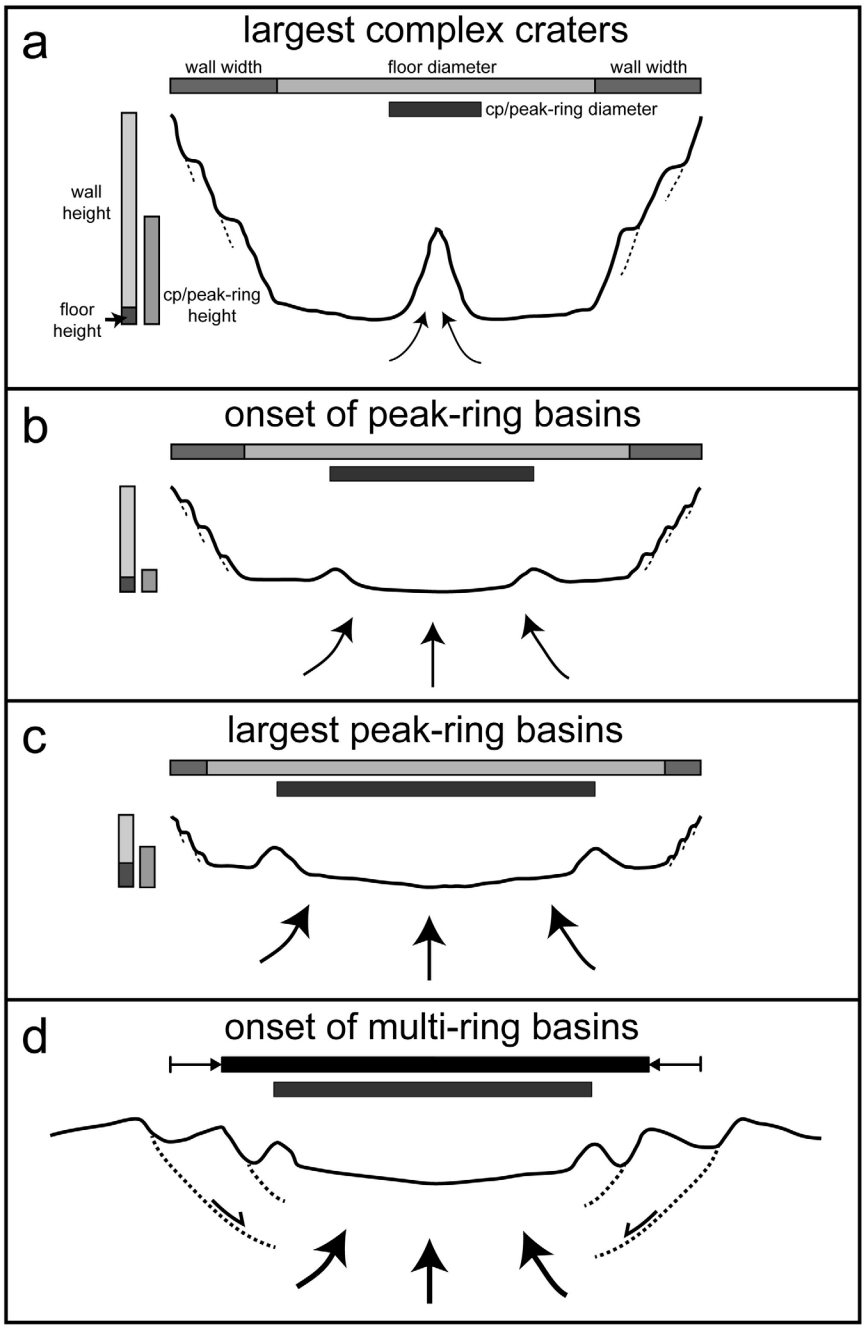

Figure 14. Diagram showing the relative changes in the geometric properties that occur in the transition from (a) complex craters to (b, c) peak-ring basins and (d) multi-ring basins. The profiles are normalized to one crater diameter for ease in comparison between craters of different sizes and calculated height and distance ratios. The lengths of the vertical and horizontal bars show the relative dimensions of geometric properties. The arrows show the zones and relative magnitudes of central uplifts. The black bar in Figure 14d illustrates the relative decrease in rim-crest diameter that may result from mega-terracing during multi-ring basin formation. A complete description and interpretation of these geometric trends are given in section 6 in the text.

suggested to occur in two major stages [*Hawke and Head*, 1977; *Osinski et al.*, 2011]. The first occurs during the final moments of the excavation stage, where a fraction of the melted target material is ejected from the excavated zone of the transient cavity. The second stage occurs when uplift of the crater floor imparts an outward momentum to the impact melt, forcing it to be re-distributed on the crater floor and to points exterior to the crater, where it may form melt flows on the continuous ejecta blanket [*Hawke and Head*, 1977; *Osinski et al.*, 2011]. It is during this stage that melt may be deposited to cover the toes of slump blocks, creating the observed sharp topographic break between the wall and

basin floor and reducing the W/r_r and h_{wall}/d ratios. This process is likely to become more important as the size of the crater and volume of melt increases, further decreasing the relative width and height of the walls and, perhaps, creating enhanced topography in the central portions of the basin from which the impact melt was expelled (section 6.4). Oblique impacts will likely have an effect on the re-distribution of impact melt by preferentially ejecting material downrange from the impact direction. Asymmetries in collapse caused by variations in preexisting and rim-crest topography and slumping are also important factors [*Hawke and Head*, 1977].

6.4. Largest Peak-Ring Basins

[61] With increasing rim-crest diameter, the d/D_r ratio for peak-ring basins continues to decrease, resulting in the largest peak-ring basins (Figure 14b) having d/D_r ratios less than a factor of two smaller than the smallest peak-ring basins (Figure 9a). This shallowing effect is less dramatic than that between complex craters and peak-ring basins and could represent continued reduction in the cratering efficiency of impact events forming peak-ring basins. This reduction in cratering efficiency and relative increase in impact melt production also results in increased impact melt retention with increasing basin size [*Cintala and Grieve*, 1998]. Re-distribution of this impact melt with the crater interior during cavity collapse has many implications for the observed basin geometries, as described below. Continued shallowing of basins could also be the result of even greater floor uplift in the largest peak-ring basins. An increase in magnitude of floor uplift is supported by the increase in height of peak rings with increasing rim-crest diameter (Figures 9c and 10b), similar to the increase in heights of central peaks within complex craters [*Pike*, 1977; *Hale and Grieve*, 1982].

[62] While the entire floor may be experiencing substantial uplift to reduce the overall basin depth, the increasing floor height to depth ratio (h_{floor}/d) for peak-ring basins (Figure 9d) suggests that the central portions interior to the peak ring are actually deepening. This floor deepening process is consistent with the observation of central depressions in some peak-ring basins (e.g., Korolev, Moscoviense and Apollo) on the Moon, on Mercury [*Baker et al.*, 2011b] and multi-ring basins on the Moon (e.g., the central depression of Orientale basin) [*Spudis*, 1993]. While the cause of these central depressions is not entirely clear, it is possible that they may be a consequence of large volumes of impact melt production and expulsion of this melt from the interior of the basin, as expected for large impact events [*Grieve and Cintala*, 1992; *Cintala and Grieve*, 1998; *Osinski et al.*, 2011]. As interpreted for the smallest peak-ring basins, the decrease in the W/r_r and h_{wall}/d ratios for peak-ring basins (Figures 10d and 10e) could reflect burial of the toes of slump blocks by re-deposition of impact melt on the basin floor. This is consistent with morphological observations, which show a general decrease in the amount of floor roughening exterior to the peak ring in peak-ring basins. The removal of melted material away from the center of the basin by the expulsion process would also act to deepen the central portions of the basin. However, thermal subsidence of the floor is thought to be responsible for at least some of the topography in the center of Orientale [*Solomon et al.*, 1982; *Bratt et al.*, 1985] and could potentially be contributing to some of the central floor deepening observed in peak-ring basins.

6.5. Onset of Multi-ring Basins

[63] The evolving geometric trends for the largest peak-ring basins are informative for evaluating the processes forming multi-ring basins (Figure 14d). To see how the trends of peak-ring basins compare with multi-ring basins, we calculated the geometric properties of the freshest multi-ring basin on the Moon, Orientale basin (19.90°S, 94.81°W), and plotted its depth and height ratios with those of proto-basins and peak-ring basins in Figures 9 and 10. Our measured ring diameters are slightly larger than the classic designations of 480, 620, and 930 km for the Inner Rook, Outer Rook, and Cordillera rings [*Wilhelms et al.*, 1987; *Spudis*, 1993]; our values are 484 km, 658, and 930 km. These differences, especially for the Outer Rook ring, are the result of our use of LOLA topography for identifying the best approximation of the crest of each ring. Although morphological arguments may favor a smaller diameter, we will use our measured values for consistency with our measurements of peak-ring basins, which are also based on topography data. Based on a collection of evidence from morphology, topography, and gravity of Orientale, the Outer Rook ring appears to best approximate the location of the rim crest of the transient cavity [*Head*, 1977; *Head et al.*, 1993]. If this is true, then the Inner Rook ring may represent the multi-ring basin equivalent of the inner peak ring of peak-ring basins [*Head*, 1977]. Thus, examining the geometric properties of the Outer Rook and Inner Rook rings in relation to the trends for peak-ring basins may help to decipher the processes controlling multi-ring basin formation.

[64] Several observations from comparisons between Orientale and peak-ring basins are apparent. First, comparisons of the diameters of the Inner Rook and Outer Rook rings show a distinct deviation from the trends of peak-ring basins. This is shown in a plot of peak-ring diameter versus rim-crest diameter (Figure 15a), where the diameter of the Inner Rook ring is much larger for its rim-crest diameter (i.e., the Outer Rook ring), when compared with a power law trend to peak-ring basins. This deviation in the peak-ring and rim-crest diameter is also apparent in the Inner Rook/Outer Rook diameter ratio (0.74), which is much larger than a peak-ring/rim-crest ratio of 0.55 for the largest peak-ring basins (Figure 15b) [*Baker et al.*, 2011a]. Second, the Outer Rook ring has a reduced depth for its diameter compared with peak-ring basins and the *Williams and Zuber* [1998] trend-line (Figure 9a). The depth of the Cordillera ring is more in-line with the peak-ring basin trend of *Williams and Zuber* [1998], while the depth of the Inner Rook ring is about 1 km shallower than expected for peak-ring basins of similar size (Figure 9a). This is also reflected in the d/D_r ratios (Figure 10a), which show the ratio of the Outer Rook ring to be slightly smaller than the trend of peak-ring basins (Figure 10a). Third, the peak-ring height to basin depth ratio for the Outer Rook ring (approximating the rim crest) and the Inner Rook ring (approximating the peak ring), is slightly smaller (~0.8) than predicted by the peak-ring basin trend (Figure 10b). Fourth, the "wall heights" for the Outer Rook ring and Cordillera rings are very small relative to their total depths (Figure 10c), which fall far off the peak-ring

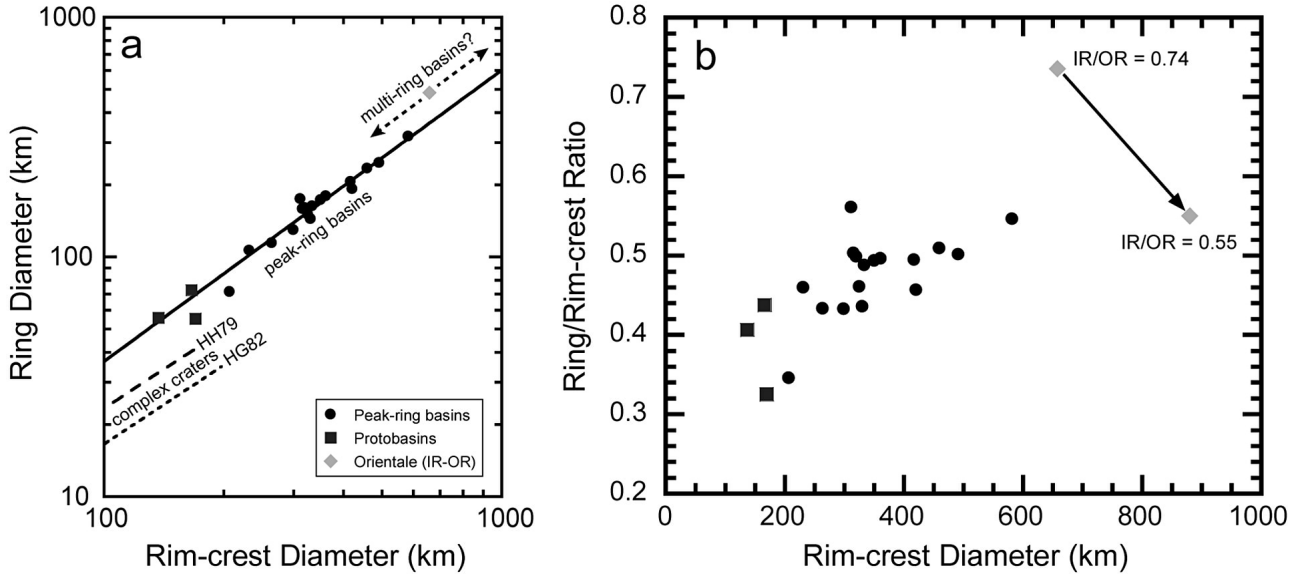

Figure 15. Peak-ring and rim-crest diameter trends for protobasins, peak-ring basins [*Baker et al.*, 2011a], and the Inner Rook (IR, diameter = 484 km) and Outer Rook rings (OR, diameter = 658 km) of Orientale, which appear to represent the multi-ring basin equivalents of a peak ring and the rim crest, respectively [*Head*, 1977]. (a) Log-log plot of the peak-ring diameter versus rim-crest diameter for protobasins (dark gray squares), peak-ring basins (black circles), and Orientale (light gray diamond). Also plotted are the diameter trends for central peaks in complex craters, as calculated by *Hale and Head* [1979] (HH79) and *Hale and Grieve* [1982] (HG82). The solid black line is a power law fit to peak-ring basins, extrapolated to the limits of the axes. The diameter of the Inner Rook ring is much larger for its rim-crest diameter (i.e., the Outer Rook ring) when compared to the power law fit to peak-ring basins. It is possible that the transition from peak-ring basins to multi-ring basins is expressed as a step in power law trends in this type of plot, similar to the jump observed in the transition from complex craters to peak-ring basins. (b) Linear-axes plot of peak-ring/rim-crest ratios for protobasins (squares), peak-ring basins (circles), and Orientale basin (light diamonds). Orientale has a much larger peak-ring/rim-crest ratio (i.e., Inner Rook/Outer Rook diameter ratio; 0.74) compared with peak-ring basins. If the Inner Rook ring diameter remains fixed, then a 34% increase in the diameter of the Outer Rook ring is needed to reduce the ratio from 0.74 to 0.55 (black arrow). The small diameter of the present Outer Rook ring could possibly be related to inward translation from mega-terracing and reduction in terracing of the Outer Rook mountains [*Head*, 1977].

basin trend on a log-log plot of the h_{wall}/d ratio. Finally, the h_{floor}/d ratio for the Outer Rook ring is more in-line with the peak-ring basin trend, with a value of about 0.5 (Figure 10d).

[65] A widely used model to explain the formation of multi-ring structures is the "mega-terrace" model [*Head*, 1974, 1977; *Spudis*, 1993]. Under this scenario, the onset of multi-ring basins occurs when the structurally uplifted portion of the rim of a would-be peak-ring basin is translated downward and inward along deep-seated listric faults to form mega-terraces (Figure 14d). For Orientale, the final resting position of this megaterrace is the equivalent to the current position of the Outer Rook ring, with the inner peak ring forming the Inner Rook ring, and the footwall of the mega-terrace forming the Cordillera ring [*Head*, 1977].

[66] The extreme translation of target materials that accompanies mega-terracing has several implications for comparisons with peak-ring basins. First, it predicts a reduction of the diameter of the transient cavity's rim crest due to inward translations from listric faulting. This reduction in diameter is apparent from the ring/rim-crest ratios of Orientale compared with peak-ring basins (Figure 15). If we use our measured ring diameters for Orientale, we calculate an Inner Rook/Outer Rook ring diameter ratio of 0.74, which is much larger than the ~0.55 peak-ring/rim-crest ratio determined for the largest peak-ring basins on the Moon (Figure 15b) [*Baker et al.*, 2011a]. If the peak-ring/rim-crest ratio holds for multi-ring basin structures, then an increase in the Inner Rook/Outer Rook ratio from 0.55 to a value of 0.74 requires about a 34% reduction in the diameter of the Outer Rook ring, assuming the Inner Rook ring diameter remains fixed. A reduction of 34% of the Outer Rook ring to form its present diameter of 658 km must have occurred during crater collapse, which could plausibly be explained by a combination of inward translation of the transient crater rim crest along listric faults and an absence of rim-wall terracing [*Head*, 1977].

[67] Second, the mega-terrace model predicts a reduction in the rim-crest elevation of the transient cavity from downward translation of the transient crater rim along listric faults. It is unclear, however, how this reduction in rim elevation is manifested in depth-diameter trends, as the diameter of the Outer Rook ring would have also decreased due to listric faulting. The Outer Rook ring of Orientale is observed to have shallower depths for its diameter compared with peak-ring basins, with a smaller d/D_r ratio (Figures 9a and 10a). This could possibly be explained if downward

translation of the transient crater rim crest was relatively greater than inward translation during mega-terracing. In addition, non-proportional scaling and growth of the excavation cavity for multi-ring basin forming events could also result in the observed shallow depths.

[68] Third, mega-terracing will also reduce the height of the rim wall as the rim-crest elevation is decreased and material is compressed into the peak ring. This process will also act to decrease the h_{wall}/d ratio and increase the h_{floor}/d ratio. The reduction in the h_{wall}/d ratio of the Outer Rook ring is readily observed in Figures 10c. Expulsion of impact melt from the central portions of the basin and deposition of this melt between the Inner Rook and Outer Rook rings (section 6.5) could also act to reduce these parameters. A high h_{floor}/d ratio of about 0.5 is also observed, which is slightly greater than extrapolation of the trend of peak-ring basins (Figure 10d) and is consistent with mega-terracing or re-distribution of impact melt.

[69] Finally, the reduction of the transient crater rim-crest elevation from mega-terracing also should result in an extreme increase in the h_{pr}/d ratio, especially if the increasing h_{pr}/d trend observed for peak-ring basins (Figure 10b) is maintained for multi-ring basins. While the h_{pr}/d ratio is greater for Orientale than for the largest peak-ring basins ($\sim$0.8 compared to $\sim$0.6), this value for Orientale is less than that predicted from extrapolation of the peak-ring basin trend (this trend predicts values approaching 1.0) (Figure 10b). Thus, it appears that the peak ring of Orientale (i.e., the Inner Rook ring) has a reduced height compared to what our peak-ring basin observations would predict. A possible reason for this smaller peak-ring height is that there is a physical limit to the height of peak rings at multi-ring basin scales, possibly related to greater gravitational instability and failure of the slopes of the ring's massifs. Little terracing of the Inner Rook ring is observed, however [*Head*, 1974], suggesting that wall failure may not be contributing to this reduction in peak-ring height.

7. Conclusions

[70] Using new high-quality topographic data provided by the Lunar Orbiter Laser Altimeter, we have developed a new technique for measuring and calculating the geometric properties of impact basins on the Moon. This new method meets a number of criteria that are important to consider in any topographic analysis of craters. These criteria include using many data points over a complete range of azimuth, being systematic so that the analysis can be readily reproduced by others, avoiding subjective biases, avoiding areas that have been obviously affected by post-impact processes, and being robust with respect to the statistical techniques used for the calculation. In particular, our data more completely capture the azimuthal variation in topography that is characteristic of large impact structures. Several new geometric trends for peak-ring basins are observed:

[71] 1) *Basin depth:* There is a factor of two reduction in the depth to diameter ratio in the transition from complex craters to peak-ring basins (Figure 9a), consistent with previous observations of impact basins on the Moon. Our depth measurements suggest that there may be a steeper trend in depth and diameter than previous studies; however, the small sample size precludes a confident interpretation of this trend. The depth/diameter ratio for peak-ring basins (Figure 10a) decreases with rim-crest diameter, which may be the result of continued reduction in cratering efficiency or increase in magnitude of floor uplift.

[72] 2) *Wall height, width, and slope:* Wall height and width increase (Figures 9d and 9e), while slope decreases (Figure 9f) with increasing rim-crest diameter. The ratios of the wall width and wall height to basin depth decrease (Figures 10c and 10e) and may reflect burial of the toes of wall slump blocks from re-distribution of impact melt during collapse of the transient cavity. Expulsion of impact melt from the central portions of the basin may help explain the observed increase in the floor height to depth ratio (Figure 10d) and is consistent with observations of central depressions within the largest peak-ring basins on the Moon and Mercury [*Baker et al.*, 2011b].

[73] 3) *Peak-ring height:* The height of the peak ring increases with increasing rim-crest diameter in a manner similar to central peak heights in complex craters, although at larger crater diameters (Figure 9c). The peak-ring height to basin depth ratio also increases (Figure 10b), suggesting that floor uplift is even larger in magnitude in the largest peak-ring basins. No correlation is found between the peak-ring elevation and distance to the rim wall within a single basin (Figures 11a and 11b), suggesting that rim-wall slumping does not exhibit a large control on the topography of peak-ring basins. There is a slight correlation between rim-crest height and peak-ring height within peak-ring basins (Figure 11c), which indicates that the pre-impact surface is important in determining the final topographic characteristics of peak rings.

[74] 4) *Offset of peak rings*: Peak rings are offset from the center of the basin by an average distance of 13 km (Table 6 and Figure 12a). From the limited number of peak-ring basins analyzed, overall we find little evidence of substantial enhancement of the peak-ring elevation in the direction of peak-ring offset (Figure 12a). This may in part be a function of offset magnitude or peak-ring preservation, as most of the peak rings in peak-ring basins on the Moon are only partially complete or have been modified by superposed impacts.

[75] 5) *Basin volume*: The volumes of peak-ring basins are, on average, $\sim$40% smaller than the volumes predicted by geophysical estimates of the dimensions of their corresponding excavation cavities (Figure 13). This difference indicates that collapse of the transient cavity must result in large inward and upward translations of the cavity floor, which must be physically explained in any model for basin formation.

[76] These new observations of the geometric properties of protobasins and peak-ring basins place some constraints on the processes controlling the onset and formation of interior landforms in peak-ring basins. Reduction in the depth to diameter ratio relative to complex craters could be due to a combination of non-proportional scaling of excavation cavity dimensions at the onset of peak-ring basins and increased uplift of the basin floor. Increased impact melting and re-distribution of this melted material within the interior of the basin could account for the decreasing ratio of wall height to depth and ratio of wall width to basin radius. More rigorous tests of the processes controlling peak-ring formation should include detailed comparisons between these new geometric relationships with proposed models of peak-ring

formation, such as hydrodynamic collapse of a central uplift structure [*Melosh*, 1982; *Collins et al.*, 2002] and interior modification from a nested melt cavity [*Cintala and Grieve*, 1998; *Head*, 2010].

[77] Furthermore, comparisons of the geometric trends of the inner rings of Orientale basin with those of peak-ring basins are generally consistent with a mega-terrace model for the formation of multi-ring basins. This suggests that brittle failure of target material and movement along large-scale faults is an important process during collapse of the transient cavity to form basin structures, which is in agreement with field observations and numerical modeling [*Spray and Thompson*, 1995; *Senft and Stewart*, 2009]. The small population of peak-ring basins on the Moon precludes more confident interpretations of the geometric trends revealed by our improved data set. Further tests of these geometric trends using the larger population of peak-ring basins on other planets, such as Mercury [e.g., *Baker et al.*, 2011b], should be made to reduce these uncertainties and to improve our model for the progression of basin shapes in the transition from complex craters to multi-ring basins.

[78] **Acknowledgments.** Thanks are extended to Jay Dickson for help in data processing. The manuscript benefited from helpful reviews by Michelle Kirchoff and an anonymous reviewer. We gratefully acknowledge financial support from the NASA Lunar Reconnaissance Orbiter Lunar Orbiter Laser Altimeter (LOLA) experiment (NNX09AM54G to JWH).

References

Alexopoulos, J. S., and W. B. McKinnon (1994), Large impact craters and basins on Venus, with implications for ring mechanics on the terrestrial planets, *Spec. Pap. Geol. Soc. Am.*, *293*, 29–50.

Araki, H., et al. (2009), Lunar global shape and polar topography derived from Kaguya-LALT laser altimetry, *Science*, *323*(5916), 897–900, doi:10.1126/science.1164146.

Baker, D. M. H., J. W. Head, C. I. Fassett, S. J. Kadish, D. E. Smith, M. T. Zuber, and G. A. Neumann (2011a), The transition from complex crater to peak-ring basin on the Moon: New observations from the Lunar Orbiter Laser Altimeter (LOLA) instrument, *Icarus*, *214*, 377–393, doi:10.1016/j.icarus.2011.05.030.

Baker, D. M. H., J. W. Head, S. C. Schon, C. M. Ernst, L. M. Prockter, S. L. Murchie, B. W. Denevi, S. C. Solomon, and R. G. Strom (2011b), The transition from complex crater to peak-ring basin on Mercury: New observations from MESSENGER flyby data and constraints on basin-formation models, *Planet. Space Sci.*, *59*, 1932–1948, doi:10.1016/j.pss.2011.05.010.

Baldwin, R. B. (1949), *The Face of the Moon*, 239 pp., Univ. of Chicago Press, Chicago, Ill.

Baldwin, R. B. (1963), *The Measure of the Moon*, 488 pp., Univ. of Chicago Press, Chicago, Ill.

Bratt, S. R., S. C. Solomon, and J. W. Head (1985), The evolution of impact basins: Cooling, subsidence and thermal stress, *J. Geophys. Res.*, *90*(B14), 12,415–12,433, doi:10.1029/JB090iB14p12415.

Cintala, M. J., and R. A. F. Grieve (1998), Scaling impact-melt and crater dimensions: Implications for the lunar cratering record, *Meteorit. Planet. Sci.*, *33*, 889–912, doi:10.1111/j.1945-5100.1998.tb01695.x.

Collins, G. S., H. J. Melosh, J. V. Morgan, and M. R. Warner (2002), Hydrocode simulations of Chicxulub crater collapse and peak-ring formation, *Icarus*, *157*, 24–33, doi:10.1006/icar.2002.6822.

Croft, S. K. (1985), The scaling of complex craters, *Proc. Lunar Planet Sci. Conf.*, *15th*, Part 2, *J. Geophys. Res.*, *90*, C828–C842.

Ekholm, A. G., and H. J. Melosh (2001), Crater features diagnostic of oblique impacts: The size and position of the central peak, *Geophys. Res. Lett.*, *28*(4), 623–626, doi:10.1029/2000GL011989.

Garrick-Bethell, I., and M. T. Zuber (2009), Elliptical structure of the lunar South Pole-Aitken basin, *Icarus*, *204*, 399–408, doi:10.1016/j.icarus.2009.05.032.

Grieve, R. A. F., and M. J. Cintala (1992), An analysis of differential impact melt-crater scaling and implications for the terrestrial cratering record, *Meteoritics*, *27*, 526–538.

Gulick, S. P. S., et al. (2008), Importance of pre-impact crustal structure for the asymmetry of the Chicxulub impact crater, *Nat. Geosci.*, *1*, 131–135.

Hale, W. S., and R. A. F. Grieve (1982), Volumetric analysis of complex lunar craters: Implications for basin ring formation, *Proc. Lunar Planet. Sci. Conf.*, *13th*, Part 1, *J. Geophys. Res.*, *87*, suppl., A65–A76, doi:10.1029/JB087iS01p00A65.

Hale, W. S., and J. W. Head (1979), Central peaks in lunar craters: Morphology and morphometry, *Proc. Lunar Planet. Sci. Conf.*, *10th*, 2623–2633.

Hartmann, W. K., and C. A. Wood (1971), Moon: Origin and evolution of multi-ring basins, *Moon*, *3*, 3–78, doi:10.1007/BF00620390.

Haruyama, J., et al. (2009), Long-lived volcanism on the lunar farside revealed by SELENE Terrain Camera, *Science*, *323*, 905–908, doi:10.1126/science.1163382.

Hawke, B. R., and J. W. Head (1977), Impact melt on lunar crater rims, in *Impact and Explosion Cratering*, edited by D. J. Roddy, R. O. Pepin, and R. B. Merrill, pp. 815–841, Pergamon Press, New York.

Head, J. W. (1974), Orientale multi-ringed basin interior and implications for the petrogenesis of lunar highland samples, *Moon*, *11*, 327–356, doi:10.1007/BF00589168.

Head, J. W. (1975), Processes of lunar crater degradation: Changes in style with geologic time, *Moon*, *12*, 299–329, doi:10.1007/BF02629699.

Head, J. W. (1977), Origin of outer rings in lunar multi-ringed basins: Evidence from morphology and ring spacing, in *Impact and Explosion Cratering*, edited by D. J. Roddy, R. O. Pepin, and R. B. Merrill, pp. 563–573, Pergamon Press, New York.

Head, J. W. (1982), Lava flooding of ancient planetary crusts: Geometry, thickness, and volumes of flooded lunar impact basins, *Moon Planets*, *26*, 61–88, doi:10.1007/BF00941369.

Head, J. W. (2010), Transition from complex craters to multi-ringed basins on terrestrial planetary bodies: Scale-dependent role of the expanding melt cavity and progressive interaction with the displaced zone, *Geophys. Res. Lett.*, *37*, L02203, doi:10.1029/2009GL041790.

Head, J. W., S. M. Murchie, J. F. Mustard, C. M. Pieters, G. Neukum, A. McEwen, R. Greeley, E. Nagel, and M. J. S. Belton (1993), Lunar impact basins: New data for the western limb and far side (Orientale and South Pole-Aitken Basins) from the first Galileo flyby, *J. Geophys. Res.*, *98*(E9), 17,149–17,181, doi:10.1029/93JE01278.

Holsapple, K. A. (1993), The scaling of impact processes in planetary sciences, *Annu. Rev. Earth Planet. Sci.*, *21*, 333–373, doi:10.1146/annurev.ea.21.050193.002001.

Howard, K. A. (1974), Fresh lunar impact craters: Review of variations with size, *Proc. Lunar Sci. Conf.*, *5th*, 61–69.

Ishihara, Y., T. Morota, R. Nakamura, S. Goossens, and S. Sasaki (2011), Anomalous Moscoviense basin: Single oblique impact or double impact origin?, *Geophys. Res. Lett.*, *38*, L03201, doi:10.1029/2010GL045887.

Kalynn, J., C. L. Johnson, G. R. Osinski, and O. Barnouin (2011), Topographic characterization of complex lunar craters with LOLA data, *Lunar Planet. Sci.*, *XLII*, Abstract 1514.

Lucchitta, B. K. (1978), Geologic map of the north side of the Moon, *U.S. Geol. Surv. Misc. Geol. Invest. Map*, *I-1062*.

McDonald, M. A., H. J. Melosh, and S. P. S. Gulick (2008), Oblique impacts and peak ring position: Venus and Chicxulub, *Geophys. Res. Lett.*, *35*, L07203, doi:10.1029/2008GL033346.

Melosh, H. J. (1982), A schematic model of crater modification by gravity, *J. Geophys. Res.*, *87*(B1), 371–380, doi:10.1029/JB087iB01p00371.

Melosh, H. J. (1989), *Impact Cratering: A Geologic Process*, 253 pp., Oxford Univ. Press, London.

Melosh, H. J., and W. B. McKinnon (1978), The mechanics of ringed basin formation, *Geophys. Res. Lett.*, *5*(11), 985–988, doi:10.1029/GL005i011p00985.

Mest, S. C., D. C. Berman, and N. E. Petro (2010), Geologic mapping of impact crater floor deposits near the lunar South Pole, *Lunar Planet. Sci.*, *XLI*, Abstract 2363.

Osinski, G. R., L. L. Tornabene, and R. A. F. Grieve (2011), Impact ejecta emplacement on terrestrial planets, *Earth Planet. Sci. Lett.*, *310*, 167–181, doi:10.1016/j.epsl.2011.08.012.

Pike, R. J. (1974), Depth/diameter relations of fresh lunar craters: Revision from spacecraft data, *Geophys. Res. Lett.*, *1*(7), 291–294, doi:10.1029/GL001i007p00291.

Pike, R. J. (1976), Crater dimensions from Apollo data and supplemental sources, *Moon*, *15*, 463–477, doi:10.1007/BF00562253.

Pike, R. J. (1977), Size-dependence in the shape of fresh impact craters on the Moon, in *Impact and Explosion Cratering*, edited by D. J. Roddy, R. O. Pepin, and R. B. Merrill, pp. 489–509, Pergamon Press, New York.

Pike, R. J. (1980), Formation of complex impact craters: Evidence from Mars and other planets, *Icarus*, *43*, 1–19, doi:10.1016/0019-1035(80)90083-4.

Pike, R. J. (1988), Geomorphology of impact craters on Mercury, in *Mercury*, edited by F. Vilas, C. R. Chapman, and M. S. Matthews, pp. 165–273, Univ. of Ariz. Press, Tucson.

Pike, R. J., and P. D. Spudis (1987), Basin-ring spacing on the Moon, Mercury, and Mars, *Earth Moon Planets*, *39*, 129–194, doi:10.1007/BF00054060.

Robinson, M. S., et al. (2010), Lunar Reconnaissance Orbiter Camera (LROC) Instrument Overview, *Space Sci. Rev.*, *150*, 81–124, doi:10.1007/s11214-010-9634-2.

Schimerman, L. A. (1973), *The Lunar Cartographic Dossier*, 359 pp., Defense Mapping Agency Aerospace Cent., St. Louis, Mo.

Schultz, P. H. (1976), Floor-fractured lunar craters, *Moon*, *15*, 241–273, doi:10.1007/BF00562240.

Schultz, P. H. (1988), Cratering on Mercury: A relook, in *Mercury*, edited by F. Vilas, C. R. Chapman, and M. S. Matthews, pp. 274–335, Univ. of Ariz. Press, Tucson.

Schultz, P. H. (1992a), Atmospheric effects on ejecta emplacement and crater formation on Venus from Magellan, *J. Geophys. Res.*, *97*(E10), 16,183–16,248, doi:10.1029/92JE01508.

Schultz, P. H. (1992b), Effect of impact angle on central peak/peak ring formation and crater collapse on Venus, in *Papers Presented to the International Colloquium on Venus*, pp. 103–104, Lunar and Planet. Inst., Houston, Tex.

Schultz, P. H., and A. M. Stickle (2011), Arrowhead craters and tomahawk basins: Signatures of oblique impacts at large scales, *Lunar Planet. Sci.*, *XLII*, Abstract 2611.

Senft, L. E., and S. T. Stewart (2009), Dynamic fault weakening and the formation of large impact craters, *Earth Planet. Sci. Lett.*, *287*, 471–482, doi:10.1016/j.epsl.2009.08.033.

Settle, M., and J. W. Head (1977), Radial variation of lunar crater rim topography, *Icarus*, *31*, 123–135, doi:10.1016/0019-1035(77)90075-6.

Settle, M., and J. W. Head (1979), The role of rim slumping in the modification of lunar impact craters, *J. Geophys. Res.*, *84*(B6), 3081–3096, doi:10.1029/JB084iB06p03081.

Smith, D. E., M. T. Zuber, G. A. Neumann, and F. G. Lemoine (1997), Topography of the Moon from the Clementine lidar, *J. Geophys. Res.*, *102*(E1), 1591–1611, doi:10.1029/96JE02940.

Smith, D. E., et al. (2010), The Lunar Orbiter Laser Altimeter investigation on the Lunar Reconnaissance Orbiter mission, *Space Sci. Rev.*, *150*, 209–241, doi:10.1007/s11214-009-9512-y.

Solomon, S. C., R. P. Comer, and J. W. Head (1982), The evolution of impact basins: Viscous relaxation of topographic relief, *J. Geophys. Res.*, *87*(B5), 3975–3992, doi:10.1029/JB087iB05p03975.

Sori, M. M., and M. T. Zuber (2011), Investigation of the relationship between subsurface structure and crater morphology of lunar impact craters from Lunar Orbiter Laser Altimeter (LOLA) observations, *Lunar Planet. Sci.*, *XLII*, Abstract 2694.

Spray, J. G., and L. M. Thompson (1995), Friction melt distribution in a multi-ring impact basin, *Nature*, *373*, 130–132, doi:10.1038/373130a0.

Spudis, P. D. (1993), *The Geology of Multi-Ring Impact Basins*, 177 pp., Cambridge Univ. Press, Cambridge, U. K., doi:10.1017/CBO9780511564581.

Stuart-Alexander, D. E. (1978), Geologic map of the central far side of the Moon, *U.S. Geol. Surv. Misc. Geol. Invest. Map*, *I-1047*.

Talpe, M. J., M. T. Zuber, M. E. Clarks, and E. Mazarico (2011), Regional cataloguing of lunar crater morphology, *Lunar Planet. Sci.*, *XLII*, Abstract 2549.

Wessel, P., and W. H. F. Smith (1991), Free software helps map and display data, *Eos Trans. AGU*, *72*, 441, doi:10.1029/90EO00319.

Whitten, J., J. W. Head, M. Staid, C. M. Pieters, J. Mustard, R. Clark, J. Nettles, R. L. Klima, and L. Taylor (2011), Lunar mare deposits associated with the Orientale impact basin: New insights into mineralogy, history, mode of emplacement, and relation to Orientale Basin evolution from Moon Mineralogy Mapper (M^3) data from Chandrayaan-1, *J. Geophys. Res.*, *116*, E00G09, doi:10.1029/2010JE003736.

Wieczorek, M. A., and R. J. Phillips (1999), Lunar multiring basins and the cratering process, *Icarus*, *139*, 246–259, doi:10.1006/icar.1999.6102.

Wilhelms, D. E., and F. El-Baz (1977), Geologic map of the east aide of the Moon, *U.S. Geol. Surv. Misc. Geol. Invest. Map*, *I-948*.

Wilhelms, D. E., K. A. Howard, and H. G. Wilshire (1979), Geologic map of the south side of the Moon, *U.S. Geol. Surv. Misc. Geol. Invest. Map*, *I-1162*.

Wilhelms, D. E., J. F. McCauley, and N. J. Trask (1987), The geologic history of the Moon, *U.S. Geol. Surv. Prof. Pap.*, *1348*, 302 pp.

Williams, K. K., and M. T. Zuber (1998), Measurement and analysis of lunar basin depths from Clementine altimetry, *Icarus*, *131*, 107–122, doi:10.1006/icar.1997.5856.

Wood, C. A., and J. W. Head (1976) Comparisons of impact basins on Mercury, Mars and the Moon, *Proc. Lunar Sci. Conf.*, *7th*, 3629–3651.

Zuber, M. T., D. E. Smith, F. G. Lemoine, and G. A. Neumann (1994), The shape and internal structure of the Moon from the Clementine mission, *Science*, *266*, 1839–1843, doi:10.1126/science.266.5192.1839.

D. M. H. Baker and J. W. Head, Department of Geological Sciences, Brown University, Box 1846, Providence, RI 02912, USA. (david_baker@brown.edu)

G. A. Neumann, Solar System Exploration Division, NASA Goddard Space Flight Center, Greenbelt, MD 20771, USA.

D. E. Smith and M. T. Zuber, Department of Earth, Atmospheric and Planetary Sciences, MIT, Cambridge, MA 02139, USA.